Editors' Suggestion

Investigation of rough-wall turbulence over barnacle roughness with increasing solidity using direct numerical simulations

Sotirios Sarakinos [*] and Angela Busse [†]
James Watt School of Engineering, University of Glasgow, Glasgow G12 8QQ, United Kingdom

(Received 23 September 2021; accepted 28 April 2022; published 16 June 2022)

Barnacle-type roughness can be considered as a hybrid form of roughness that combines some of the topographical features of traditional regular rough surfaces composed of discrete roughness elements of uniform size and shape, and of irregular rough surfaces that exhibit features with a wide distribution of sizes and shapes, covering the surface with a random areal distribution. In this study, the influence of barnacle-type rough surfaces with increasing coverage on wall-bounded turbulence is investigated using direct numerical simulations of turbulent channel flow. The barnacle-type rough surfaces were generated with an algorithm that mimics the settlement behavior of barnacles, and the set of seven different surfaces describe the evolution of barnacle fouling with increasing coverage ranging from a lightly fouled surface with small isolated barnacle clusters (10% coverage) to a surface that is fully covered by barnacles (85% coverage). The roughness function recovers the expected trend with frontal solidity, attaining its maximum at a frontal solidity of approximately 0.2. Mean flow, Reynolds stress, and dispersive stresses show signatures of the clustering of roughness features, i.e., the barnacle colonies, at low coverage. This is most distinct for the streamwise Reynolds stresses where a double peak is observed at the lowest coverage; the inner peak can be interpreted as a partial recovery of smooth-wall behavior over the large connected unfouled sections of this surface. The flow over the rough surfaces is further investigated by a topographical characterization of the blanketing layer, i.e., the effective shape of the rough surface "perceived" by the outer flow. A linear relationship between the roughness function and the effective slope of the blanketing layer is observed.

DOI: 10.1103/PhysRevFluids.7.064602

I. INTRODUCTION

The accumulation of marine organisms on surfaces submerged in sea water is collectively termed marine biofouling [1]. Its negative effect on the performance of sea-faring vessels has been known since ancient times, while the use of coatings as antifoulants has been recorded since the early 17th century [2]. The use of poisonous chemicals in antifoulants, such as dichlorodiphenyltrichloroethane and arsenic, led to their ban in the 1960s and their replacement by tributyltin- (TBT) based coatings [3]. However, TBT's negative effects on the environment were also severe, leading to the reduction of its use in antifoulants during the 1980s and 1990s and, finally, to its international ban in 2008 [4]. This ban has led to increased interest in the investigation of marine biofouling and its negative effects on marine vehicles and human-made structures.

Marine biofouling is primarily categorized into microfouling and macrofouling. The former includes bacteria-sized organisms and inorganic matter in particulate form that compose a thin film

[*] Sotirios.Sarakinos@glasgow.ac.uk
[†] Angela.Busse@glasgow.ac.uk

of slime, termed biofilm [2]. The latter includes all types of biofouling organisms visible to the naked eye, such as sea-squirts (*Ascidiacea*), sea-mats (*Bryozoa*), hydroids (*Hydrozoa*), mussels (*Bivalvia*), tube-worms (*Serpulidae*), and barnacles (*Cirripedia*) [5]. Both microfouling and macrofouling have been found to increase frictional resistance of substrate surfaces [6,7]; however, the effect caused by calcareous macrofouling is considered to be the most severe [8–10], and sessile barnacles (*Sessilia*) are some of the most dominant biofouling species [11].

The main harmful effect of marine biofouling is the increased roughness of underwater surfaces, where the biofouling organisms settle, resulting in a decrease of vehicle speed and increased power requirements [12]. Biofouling can also affect propellers and the blades of wave and tidal turbines, reducing their efficiency by increasing their effective diameters, leading to increased drag and inertia loads [13–15]. Further adverse effects linked to the accumulation of marine organisms on surfaces are the destruction of coatings and increased corrosion. The significant economic impact of biofouling can be illustrated by a practical example given by Schultz *et al.* [16] who estimated that the fuel consumption of a US Navy Arleigh-Burke-class destroyer increases by 20.4% at a fouling rating of 60, which corresponds to a surface affected by small calcareous fouling or weeds.

The increase in frictional resistance of submerged surfaces due to calcareous marine biofouling has been studied both through experimental investigations and numerical simulations of the flow over representative rough surfaces [7,17–19]. For example, Schultz [8] performed towing tank experiments to investigate the drag resistance of metal test plates with different coatings that were exposed to a biofouling environment for over nine months. The experiments showed that while in an unfouled state all plates performed similarly, for the fouled plates the Hama roughness function ΔU^+ [20] increased with increasing coverage by biofouling. Monty *et al.* [10] investigated the flow over a sparsely biofouled surface with light calcareous tube-worm fouling using wind tunnel experiments. The surface was obtained from a three-dimensional (3D) scan of a plate that had been exposed for two months to a biofouling environment. Compared to the experiments by Schultz, the equivalent sand-grain roughness of their surface was found to be similar to that of heavy biofilm coatings but lower than the lightly fouled cases investigated by Schultz [8].

The process of obtaining real marine biofouling specimens can be time-consuming and costly, since the test plates have to be exposed to sea-water conditions for several months to accumulate organisms, and it is difficult to exactly control the type and amount of settling organisms. Therefore, artificially created forms of marine roughness are also used for the investigation of the fluid dynamic effects biofouling [9,18,21,22] where typically barnacle-shaped roughness elements of uniform size are placed in regular or staggered arrangements to create rough surfaces with well-controlled roughness height, surface coverage, and frontal solidity. However, natural barnacle-fouled surfaces exhibit neither a perfectly uniform height distribution due to natural variations in barnacle size nor a perfectly regular arrangement of the barnacles, since barnacles tend to settle next to each other and form colonies. These properties are also exhibited by other forms of roughness with discrete features, e.g., urban roughness is often formed of buildings of various heights that are distributed in a nonuniform pattern, and surface pitting corrosion typically originates from localized sites which subsequently grow to affect the surrounding surface area [23].

Barnacle-type roughness, and similar types of rough surfaces with randomly sized roughness features in nonuniform clustered arrangements, can be considered hybrid forms of roughness that fall into the range between the widely studied artificial regular rough surfaces formed of regular arrangements of uniformly sized roughness elements, such as cubes or hemispheres (see, e.g., Refs. [24–28]), and general irregular forms of roughness with a uniformly random spatial distribution of roughness features (see, e.g., Refs. [29–36]). The investigation of realistic barnacle-type roughness is therefore not only of interest in the context of marine biofouling but can also serve as a useful example for a class of roughness that falls into the spectrum between discrete versus distributed and regular versus irregular forms of roughness that have been the focus of most previous investigations of the topography-dependence of rough-wall turbulence.

In the current study, the effect of a set of barnacle-type rough surfaces with increasing coverage on wall-bounded turbulence is investigated using direct numerical simulations. All surfaces have

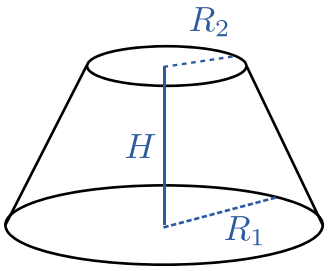

FIG. 1. Representation of the barnacle geometry as a conical frustum following Sadique [22]. H, barnacle height; R_1, base radius; and R_2, upper radius.

been created with an algorithm that mimics the gregarious behavior of barnacles resulting in rough surfaces, with clustered features composed of barnacle-shape roughness elements with a realistic distribution of sizes (see Sec. II A). Direct numerical simulations of turbulent channel flow at $\mathrm{Re}_\tau = 395$ were used to obtain mean flow and turbulence statistics for each surface (Sec. II B). Results for the roughness function are discussed in relation to frontal solidity and effective slope in Sec. III A. Mean flow, Reynolds, and dispersive stress statistics are discussed in Secs. III B and III C. A detailed investigation of the mean flow field in the vicinity of the rough surfaces (see Secs. III D and III E) shows that the increase and subsequent drop in fluid dynamic roughness effect with increasing coverage can be related to changes in the flow patterns within the rough surfaces and the topography of the blanketing layer that forms above the roughness. Conclusions are given in Sec. IV.

II. METHODOLOGY

The aim of the current study is to investigate the dependence of the roughness function and the statistical properties of the near-wall flow on the degree of coverage by barnacles, a typical form of calcareous macro-fouling encountered in marine environments. Surface coverage is known to be a key parameter in the context of marine biofouling [8]. Seven different rough surfaces were generated with an algorithm that mimics the settlement behavior of barnacles. For each surface, a direct numerical simulation of rough-wall turbulent channel flow was conducted to obtain its effect on the mean flow and turbulence properties.

A. The surfaces

Barnacles are a species of arthropods that belong to the taxon of *Crustacea*. The order *Sessilia* [2], commonly known as acorn barnacles or sessile barnacles [37], is the most typical form found in marine biofouling. The acorn barnacle settlement behavior has been well documented [38–42]. Most researchers agree that acorn barnacles prefer to form colonies and settle in places where mature barnacles of the same species have already settled [38,39]. In the current study, rough surfaces were generated with an algorithm that mimics this gregarious behavior of barnacles [43]. Barnacles are modelled as conical frustra (see Fig. 1) following the approach by Sadique [22], and a realistic distribution of barnacle shapes and sizes is used (see Table I). Starting from a set of seed barnacles,

TABLE I. Geometric properties of the barnacles used to generate the rough surfaces: R_1, base radius; RR, ratio of upper to lower radius; AR, aspect ratio.

	R_1 (mm)	R_1/δ	RR	AR
Minimum	3.5	0.0880	0.31	0.34
Maximum	6	0.1508	0.4	0.42

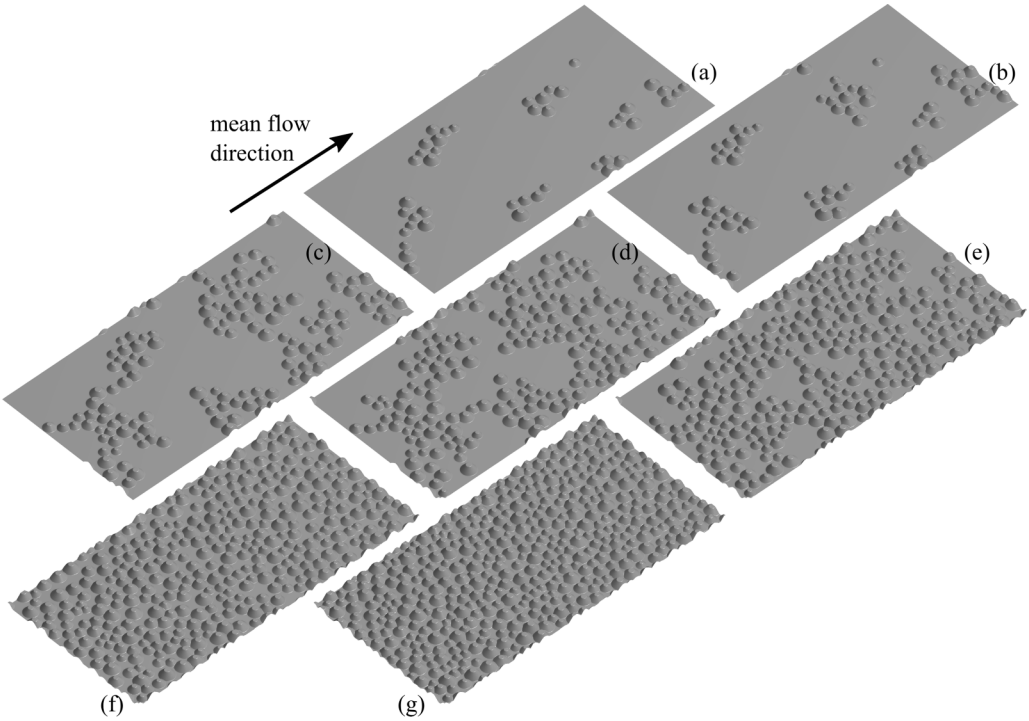

FIG. 2. Visualization of all rough surfaces in order of increasing coverage by barnacles: (a) 10% coverage, (b) 15% coverage, (c) 30% coverage, (d) 45% coverage, (e) 60% coverage, (f) 75% coverage, and (g) 85% coverage.

additional barnacle shapes are placed successively on a flat surface in the vicinity of other already settled barnacles, mimicking their tendency to form colonies [see Fig. 2(a)]. By gradual addition of further barnacles the coverage of the surfaces is increased [see Figs. 2(b) to 2(f)] until no further barnacles can be placed and the maximum coverage is attained [see Fig. 2(g)].

In total, seven surfaces were generated at 10%, 15%, 30%, 45%, 60%, 75%, and 85% coverage. Each coverage state is derived from the previous one by adding more barnacles in order to achieve the desired coverage percentage, thus realizing the evolution of a barnacle colony.

The size of the original surface was 250 mm $\times$ 125 mm and the barnacles' geometric characteristics were based on the ranges given by Sadique [22]. AR denotes the aspect ratio of the barnacle, defined as the ratio of height H over base diameter $2R_1$, and RR is the ratio of the upper radius R_2 to the base radius R_1 (see Table I). To maintain a constant reference roughness height for all the surfaces, the geometry of the first barnacle was defined with the maximum value for H.

The topographical properties of all rough surfaces are presented in Table II. For the direct numerical simulations all surfaces were nondimensionalized based on the mean channel half-height δ. The streamwise extent of the flow domain ℓ_x was set to $2\pi\delta$, with the spanwise extent $\ell_y = \pi\delta$. This yields a maximum peak-to-valley height of $S_{z,\max}$ of 0.1267δ for all surfaces. This is essentially the height of the first barnacle added on the surface and will be used as a reference roughness height in the following. The height of the smallest barnacle in the population varies slightly due to the random nature of the surfaces dropping from 0.0684δ for the 10% surface to 0.0603δ for the 85% surface. In the following, the latter will be referred to as "minimum barnacle height."

The topographical parameters change with increasing coverage (see Table II), most notably skewness and kurtosis of the roughness height distribution (see Fig. 3). The solid line in Fig. 3

TABLE II. Topographical parameters of the barnacle surfaces. N_b, number of barnacles; λ_f, frontal solidity; ES, effective slope, S_a, mean roughness height; S_q, rms roughness height; S_{sk}, skewness; S_{ku}, kurtosis; L^x_{corr}, streamwise correlation length, L^y_{corr}, spanwise correlation length; z_0, smooth-wall displacement.

Coverage	N_b	λ_f	ES	S_a/δ	S_q/δ	S_{sk}	S_{ku}	$L^x_{\mathrm{corr}}/\delta$	$L^y_{\mathrm{corr}}/\delta$	z_0/δ	Line style
10%	44	0.033	0.067	0.0089	0.0180	4.06	19.5	0.26	0.19	−0.0049	
15%	66	0.050	0.099	0.0126	0.0214	3.16	12.4	0.28	0.31	−0.0074	
30%	135	0.102	0.204	0.0219	0.0289	1.87	5.36	0.16	0.23	−0.0153	
45%	202	0.146	0.294	0.0265	0.0321	1.31	3.48	0.13	0.13	−0.0219	
60%	275	0.198	0.397	0.0292	0.0341	0.88	2.52	0.11	0.11	−0.0296	
75%	345	0.245	0.489	0.0295	0.0343	0.58	2.15	0.095	0.095	−0.0367	
85%	440	0.276	0.553	0.0277	0.0326	0.40	2.11	0.087	0.087	−0.0421	

represents the lower bound for kurtosis based on Pearson's inequality [44]:

$$S_{\mathrm{ku}} \geqslant S_{\mathrm{sk}}^2 + 1. \tag{1}$$

For low-coverage states, skewness and kurtosis acquire high values due to the sparseness of the roughness elements and the corresponding $(S_{\mathrm{sk}}, S_{\mathrm{ku}})$ points on the skewness-kurtosis map fall close to the outer boundary imposed by Pearson's inequality. Since the roughness elements are tapering and the roughness elements have a distribution of heights, the $(S_{\mathrm{sk}}, S_{\mathrm{ku}})$ points, however, do not coincide with the inequality's boundary, since this would require height distributions that are Bernoulli distributions, as found for surfaces constructed using nontapering roughness elements of uniform height such as cubes or cylindrical posts. With increasing surface coverage, skewness, and kurtosis reduce; the skewness remains positive for all surfaces, but the kurtosis drops below 3 for the densely populated surfaces, i.e., negative excess kurtosis values are attained at coverage of 60% and above.

In the context of empirical roughness correlation the frontal solidity λ_f and effective slope $ES = 2\lambda_f$ values are also of particular interest [45,46]. These naturally increase with the placement

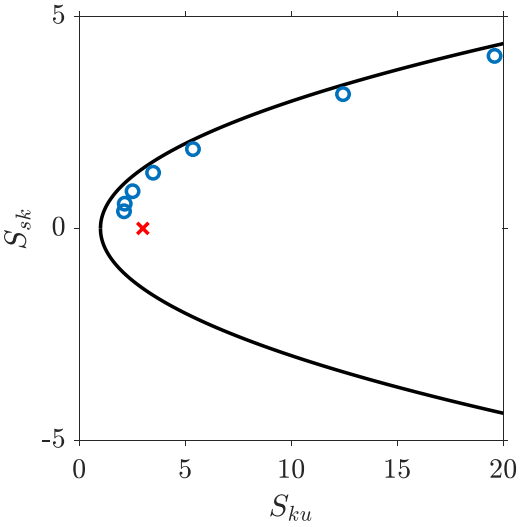

FIG. 3. Skewness plotted versus kurtosis of barnacle covered surface roughness (blue circles). The solid line marks the boundary of Pearson's inequality $S_{\mathrm{ku}} = S_{\mathrm{sk}}^2 + 1$; the red cross indicates the values for a Gaussian height distribution ($S_{\mathrm{sk}} = 0,\ S_{\mathrm{ku}} = 3$).

TABLE III. Grid and domain sizes used for the rough and the smooth-wall simulations. ℓ_x, domain size in streamwise direction; ℓ_y, domain size in spanwise direction; N_x, N_y, and N_z, number of grid points in streamwise, spanwise, and wall-normal direction; Δx^+, Δy^+, uniform grid spacing in the streamwise and spanwise direction; Δz^+_{min}, minimum wall-normal grid spacing; Δz^+_{max}, maximum wall-normal grid spacing.

Type	ℓ_x/δ	ℓ_y/δ	N_x	N_y	N_z	Δx^+	Δy^+	Δz^+_{min}	Δz^+_{max}
Rough	2π	π	864	432	512	2.87	2.87	0.67	$\leqslant 3.98$
Smooth	8	4	640	320	360	4.94	4.94	0.50	3.98

of more barnacle shapes on the smooth reference surface. The correlation between the effect of roughness on fluid flows and λ_f and ES is discussed in Sec. III A. Womack *et al.* [47] found for uniform random distributions of roughness elements that the exact placement of roughness features has negligible influence on the roughness effect.

B. Direct numerical simulations

The embedded boundary method code iIMB [48] was used for the direct numerical simulation of turbulent channel flow over the rough surfaces. The code employs second-order central differences on a staggered grid to evaluate the spatial derivatives of the incompressible Navier-Stokes equations and a second-order Adams-Bashforth method for the temporal discretization. The rough walls are resolved with an iterative version of the embedded boundary method by Yang and Balaras [49], a non-boundary-conforming method for simulating turbulent flows over complex boundaries on Cartesian grids.

Periodic boundary conditions are employed in the streamwise and spanwise direction. The rough-wall boundary conditions are applied to both the upper and the lower channel wall, with the rough surface at the upper wall shifted by half the domain size in the spanwise and streamwise direction to minimize local blockage effects. By applying a small offset z_0 to the smooth-wall plane on which the barnacles are settled, the mean roughness height of each surface is set to zero, thus defining the wall-normal coordinate $z = 0$ at the location of the roughness mean plane for each simulation, which is consistent with the approach used in several previous studies on topography-dependence of rough-wall turbulence [32,48,50,51].

The simulation parameters are summarized in Table III. The parameters for the smooth-wall reference case are also given in Table III. Uniform and dense grid spacing is employed in the streamwise (x-) and spanwise (y-) directions in all rough-wall cases to resolve the complex geometries of the irregular barnacle surfaces. In the wall-normal (z-) direction uniform spacing Δz^+_{min} is used within the roughness layer, i.e., in the range between the smooth settling plane and the highest barnacle height, and the grid is gradually stretched above attaining a maximum spacing of Δz^+_{max} at the channel center. All simulations were performed at the same friction Reynolds number $\text{Re}_\tau = 395$ with a constant mean streamwise pressure gradient. Time averages were taken over at minimum of 70 flow-through times (ℓ_x/U_b) under fully developed flow conditions. All mean flow, Reynolds, and dispersive profiles presented in the following are obtained using intrinsic averaging, i.e., averages are taken over the fluid-occupied areas.

III. MEAN FLOW STATISTICS

In this section the roughness function's dependency on the frontal solidity and effective slope is presented (see Sec. III A), followed by a discussion of the mean velocity profile in Sec. III B, and the Reynolds and dispersive stress profiles in Sec. III C. In last two subsections, the structure of the time-averaged flow field within and in the vicinity of the rough surfaces will be discussed based on the probability density functions of the local time-averaged streamwise velocity (see Sec. III D) and the statistics of the blanketing layer that forms over the rough surface (see Sec. III E).

TABLE IV. Centerline velocity, bulk flow velocity, and roughness function value for all surfaces at $\mathrm{Re}_\tau = 395$. Estimates for the equivalent sand-grain roughness k_s^{est} were obtained from the ΔU^+ values using the approach described in Chung *et al.* [46].

% Coverage	U_c/u_τ	U_b/u_τ	ΔU^+	$k_s^{\mathrm{est}}/S_{z,\max}$
10	15.42	12.84	4.87	0.57
15	14.21	11.68	6.09	0.92
30	12.96	10.44	7.33	1.52
45	12.57	10.04	7.72	1.77
60	12.40	9.82	7.89	1.90
75	12.81	10.07	7.48	1.61
85	13.22	10.51	7.08	1.37

A. Roughness function

The Hama roughness function ΔU^+ is defined as the downward shift in mean streamwise velocity profile for a rough wall compared to the smooth-wall equivalent at the same friction Reynolds number [20]. In the current study, ΔU^+ was computed by subtracting the centerline velocity values of the rough-wall cases from the smooth-wall reference case consistent with the approach used in Refs. [32,36,51] since an excellent collapse was observed for the velocity defect profile above the roughness layer [see Sec. III B]. The roughness function values, the centerline velocity, and the bulk velocity values are presented in Table IV. The roughness function values for the 10% and 15% cases fall into the upper transitionally rough region, whereas the higher-coverage states can be considered fully rough based on their ΔU^+ values.

Figure 4(a) shows the roughness function as a function of frontal solidity λ_f. With the increase in surface coverage and thus frontal solidity, ΔU^+ is increasing, attaining its maximum at 60% coverage and a frontal solidity value of approximately 0.2. Beyond this point ΔU^+ is decreasing

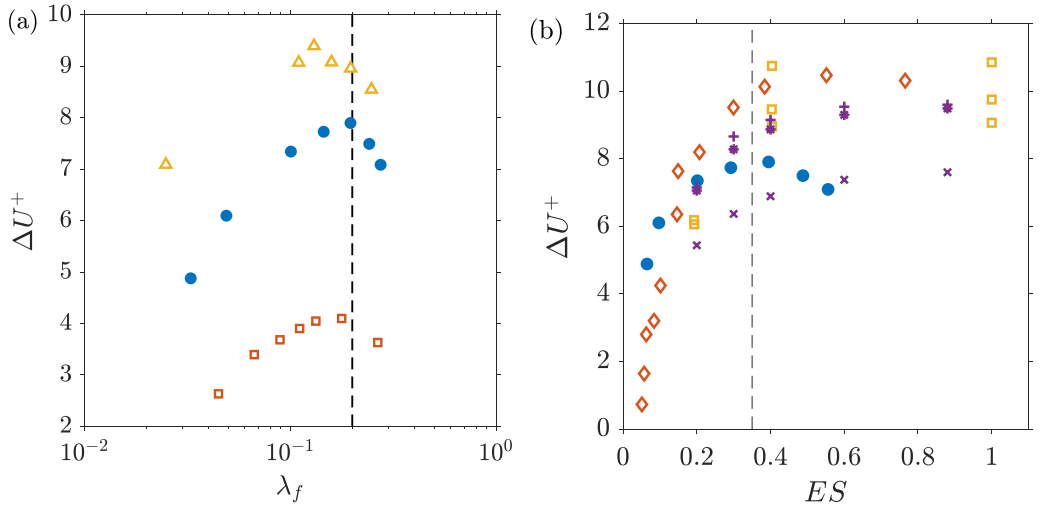

FIG. 4. (a) Roughness function ΔU^+ against surface frontal solidity λ_f (blue filled circles); data by MacDonald *et al.* [52] (orange squares) and Leonardi and Castro [26] (yellow triangles) is shown for comparison. (b) ΔU^+ against surface effective slope ES (blue filled circles). Data by Napoli *et al.* [45] (orange diamonds), Schultz and Flack [53] (yellow squares), and Forooghi *et al.* [33] (purple symbols, $+$: $S_{\mathrm{sk}} \approx 0.2$, $*$: $S_{\mathrm{sk}} \approx 0.67$, $\times$: $S_{\mathrm{sk}} = -0.33$) is shown for comparison.

for the surfaces at 75% and 85% coverage. The increase of the roughness function values for low coverage can be attributed to the increase of the number of roughness elements on the surface. For high coverage, sheltering effects become of increasing importance, which can explain the decreasing trend that is observed for coverage above 60%. For comparison, roughness function values from MacDonald *et al.* [52] for regular sinusoidal egg-carton roughness and from Leonardi and Castro [26] for regular cube roughness are also shown in Fig. 4. The overall behavior of the roughness function with respect to the surface frontal solidity is similar, although the peak is found at different λ_f values.

A similar dependence of the roughness effect on solidity has been observed in a number of other studies. Jiménez [54] collated results from the experiments by Schlichting [24], Webb *et al.* [55], Tani [56], and Bandyopadhyay [57] and found that the maximum value of the roughness function was attained at $\lambda_f \approx 0.15$ in most cases. More recently, MacDonald *et al.* [52] suggested that the critical frontal solidity value is in the region $0.15 \leqslant \lambda_f \leqslant 0.2$, based on their own results that placed the maximum at 0.18 and on the results by Placidi and Ganapathisubramani [58], who found a maximum bulk drag at $\lambda_f = 0.21$. The maximum location for the barnacle surfaces at $\lambda_f \approx 0.2$ therefore falls within the expected range.

As discussed above, frontal solidity and effective slope of a surface are directly related. In Fig. 4(b) the results from the barnacle covered surfaces are compared to those by Napoli *et al.* [45], Schultz and Flack [53], and Forooghi *et al.* [33], who performed simulations or experiments over rough surfaces with increasing effective slope. Napoli *et al.* [45] performed simulations over 2D wavy rough surfaces generated by superposition of sinusoidal functions with random amplitude which had no dependency on the spanwise direction. Their surfaces show an increase in the effective slope but, based on their definition, maintain approximately zero skewness. Schultz and Flack [53] performed experiments of turbulent channel flow over pyramid shaped roughness at several inclination angles and heights, altering the rough surfaces' effective slope while maintaining a constant positive skewness. Finally, Forooghi *et al.* [33] used artificially generated irregular rough surfaces with systematically varied parameters; from their data three different series with different skewness values (A00 series with $S_{\mathrm{sk}} \approx 0.2$, B70 series with $S_{\mathrm{sk}} \approx -0.34$, and C70 series with $S_{\mathrm{sk}} \approx 0.67$) are shown. For all the above data sets, a very similar trend is observed—an increase in the roughness function for low effective slope and an approximate saturation of the roughness effect for $ES \gtrapprox 0.35$.

Comparing to the results from the barnacle covered surfaces, a similar increase is observed up to an effective slope value of $ES \approx 0.4$ (corresponding to 60% coverage). However, as ES is increased further, a drop in ΔU^+ is observed, unlike the saturation that is seen for the other data sets. One factor that is likely to contribute to this deviation from the expected saturation with ES is that for the barnacle surface the skewness drops as ES increases. The cases with the highest effective slope have the lowest skewness, which is in line with the empirical relationship of Flack *et al.* [59] where a decrease in the roughness effect with decreasing (positive) skewness is predicted. For the data of Leonardi and Castro [26] a similar drop at high ES would be observed, since for cube roughness surface skewness also decreases with increasing planform and frontal solidity. However, surface skewness may not be the only contributing factor, as in the data of MacDonald *et al.* [52] also a drop in ΔU^+ is observed for high frontal solidity and high effective slope even though their sinusoidal egg-carton surfaces are all neutrally skewed.

Next to the frontal solidity/effective slope, skewness is probably the most widely investigated topographical roughness parameter. Flack *et al.* [59] developed the following empirical relationship for predicting the equivalent sand-grain roughness k_s based on the root-mean-square roughness height S_q and the surface skewness S_{sk}:

$$k_s^{\mathrm{pred}} = aS_q(1 + S_{\mathrm{sk}})^b, \tag{2}$$

where the constants a and b depend on whether the surface is positively, neutrally, or negatively skewed. Since the present surfaces cover a wide range of skewness, it is of interest whether their

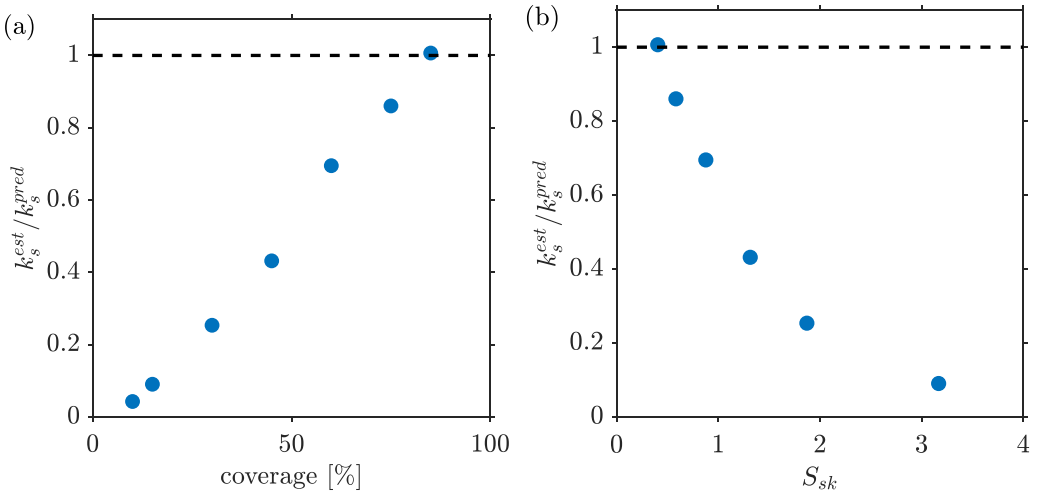

FIG. 5. Ratio of estimated to predicted equivalent sand-grain roughness vs (a) coverage and (b) skewness. The black dashed line indicates the ratio for a perfect prediction.

roughness effect shows a similar skewness dependency as predicted by the empirical relationship (2). We estimated the approximate equivalent sand-grain roughness of the surfaces based on ΔU^+ using the approach described in Chung *et al.* [46]

$$\frac{k_s^{\text{est}}}{S_q} = \frac{\exp\{\kappa[\Delta U^+ - A + B_s(\infty)]\}}{S_q^+}, \tag{3}$$

where $\kappa \approx 0.4$ and $A - B_s(\infty) \approx -3.5$.

Figure 5 shows the ratio of the estimated equivalent sand-grain roughness to the predicted equivalent sand-grain roughness using $a = 2.48$ and $b = 2.24$ as fitted by Flack *et al.* [59] for positively skewed surfaces. For the highest coverage, the predicted and the estimated equivalent sand-grain roughness agree well. However, this is not the case for the lower coverages, where there is a significant overprediction of the equivalent sand-grain roughness which worsens as the coverage decreases. Overall, the empirical relationship (2) appears to work well for moderate skewness values but fails to give a good prediction for the highly skewed surfaces. This can be attributed to the fact that this empirical relationship was developed based on data for moderately skewed surfaces $S_{\text{sk}} \lessapprox 1$.

B. Mean velocity profile

The mean streamwise velocity profile, presented in Fig. 6(a), clearly shows the increase and the subsequent decrease in the roughness function beyond 60% coverage. All profiles show approximately logarithmic behavior [51,60] above $z^+ \approx 60$, i.e., closely above the maximum barnacle height. The velocity defect profile [see Fig. 6(b)] shows an excellent collapse of all profiles on the smooth-wall case above $z/\delta \approx 0.15$ indicating that outer-layer similarity is recovered in all cases. In the near-wall region, clear differences can be observed between the roughness cases. Within the roughness layer, the mean streamwise velocity decreases with increasing coverage [see Fig. 7(a)]. In the upper part of the roughness layer, the 85% coverage case deviates from this trend and exhibits a more rapid increase in the mean streamwise velocity than the 60% and 75% coverage cases resulting in the lower roughness function measured for this case. For cases with low to moderate coverage, a relatively uniform rate of increase in the mean streamwise velocity profile can be observed over the upper part of the roughness layer [see Fig. 7(b)]. In contrast, an inflection point emerges for the cases with higher coverage. This inflection point falls between the maximum and minimum

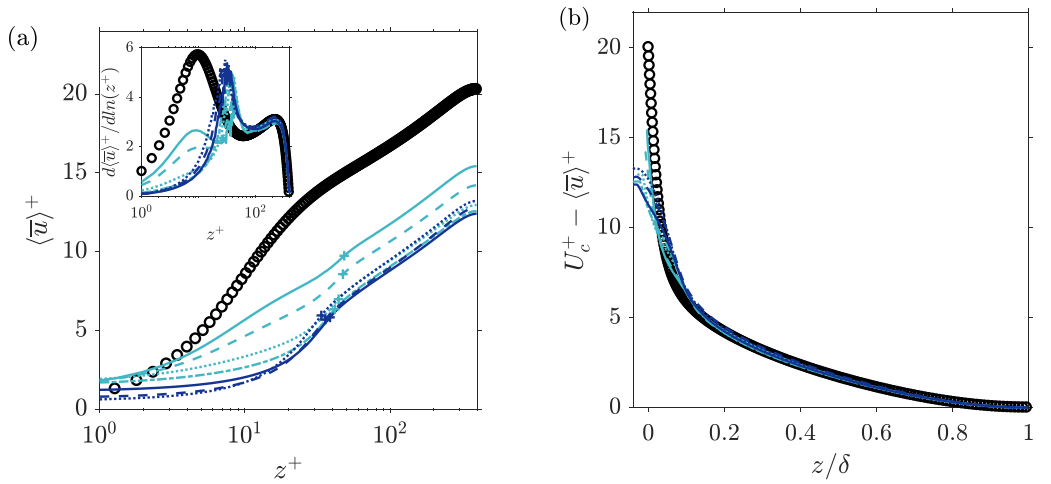

FIG. 6. (a) Mean streamwise velocity profiles of all coverage cases; the crosses indicate the maximum barnacle height, and the inset plot shows the profile differentiated with respect to $\ln(z^+)$; (b) mean velocity defect profile. Line styles for the different coverage cases are given in Table II; black circles indicate smooth-wall data.

barnacle height and becomes more pronounced as surface coverage increases. Inflection points have been observed for the streamwise velocity profile for turbulent boundary layers over plant canopies [61] and in turbulent channel flow over regular sparse canopies [62]. A similar feature can also emerge when roughness is modelled using the parametric forcing approach [63,64].

At high coverage the mean streamwise velocity deep within the rough surface decreases, with the appearance of weak net reverse flow $\langle\overline{u}\rangle < 0$ at 75% and 85% coverage within the lower part of the roughness layer leading to a stronger retardation of the flow within the lower part of the roughness layer compared to the flow in its upper part. Above the rough surface, the derivative

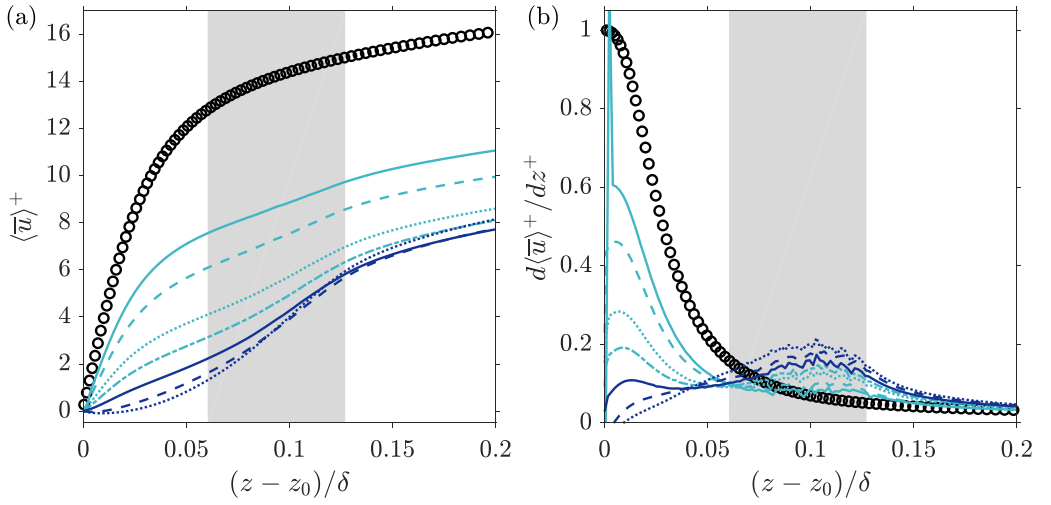

FIG. 7. (a) Mean streamwise velocity profiles close to the wall; (b) linear derivatives of the same profiles. Line styles for the different coverage cases are given in Table II; black circles indicate smooth-wall data. The areas shaded in gray indicate the range of barnacle heights.

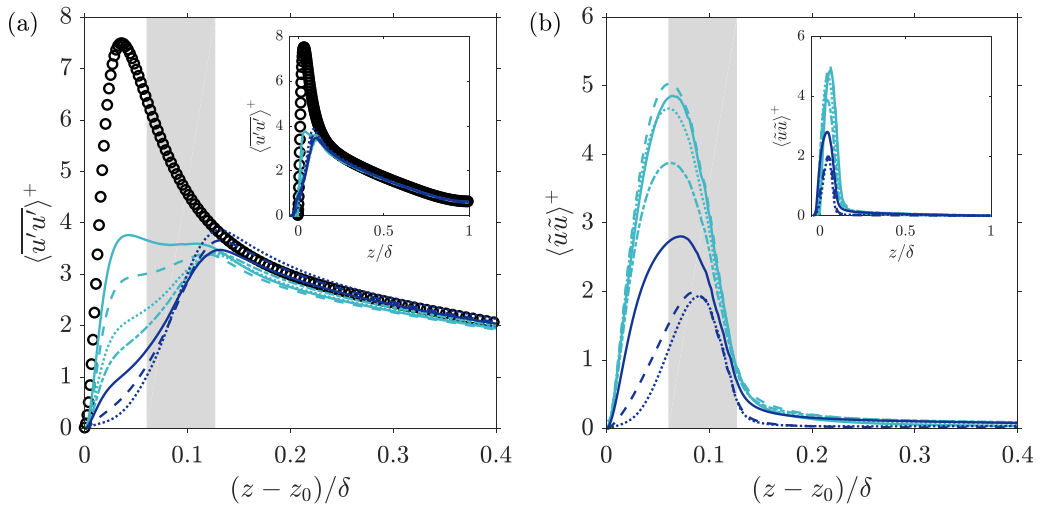

FIG. 8. Streamwise Reynolds (a) and dispersive stresses (b). The area shaded in gray indicates the range of barnacle heights. Line styles for the different coverage cases are given in Table II; black circles indicate smooth-wall data. The areas shaded in gray indicates the range of barnacle heights.

of the mean velocity profile soon collapses on the values for the smooth-wall case, indicating that direct roughness effects impact the mean flow profile only in the immediate vicinity of the rough surface.

C. Reynolds and dispersive stresses

The presence of roughness induces spatial inhomogeneities in the turbulent flow field near the wall, marking a region termed the roughness sublayer [65]. To investigate the flow properties in this region, we apply the triple decomposition of Raupach and Shaw [66]. For the u component of the velocity field this gives

$$u(x, y, z, t) = \langle \bar{u} \rangle(z) + \tilde{u}(x, y, z) + u'(x, y, z, t), \tag{4}$$

where $\langle \bar{u} \rangle(z)$ is the time and plane-averaged streamwise velocity component of the velocity field, $\tilde{u}(x, y, z) = \bar{u}(x, y, z) - \langle \bar{u} \rangle(z)$ is the spatial variation in the time-averaged streamwise velocity, and $u'(x, y, z, t) = u(x, y, z, t) - \bar{u}(x, y, z)$ denotes the instantaneous fluctuation of u around the local time-averaged value of the velocity field. The decomposition of the spanwise, v, and wall-normal, w, components of the velocity field is analogous. In the time- and plane-averaged Navier-Stokes equations, the local turbulent fluctuations give rise to the Reynolds stresses $\langle \overline{u'u'} \rangle$, $\langle \overline{u'w'} \rangle$, etc., while the roughness-induced spatial variations in the time-averaged flow field induce the dispersive stresses $\langle \tilde{u}\tilde{u} \rangle$, $\langle \tilde{u}\tilde{w} \rangle$, etc.

The Reynolds and dispersive stresses are shown in Figs. 8–11. The Reynolds stress profiles collapse in the outer part of the flow onto the smooth-wall data, and no significant dependency on the degree of surface coverage is observed [see inset panels in Figs. 8(a) to 11(a)]. The following discussion therefore focuses on the behavior of the Reynolds and dispersive stress profiles within and in the near vicinity of the rough surface (see main panels in Figs. 8–11).

Below the highest barnacle height, the streamwise normal Reynolds stress [see Fig. 8(a)] shows for all coverages a reduction in magnitude compared to the smooth-wall reference case, decreasing with increasing coverage. This is consistent with the decrease of the mean flow velocity within the rough surface with increasing coverage.

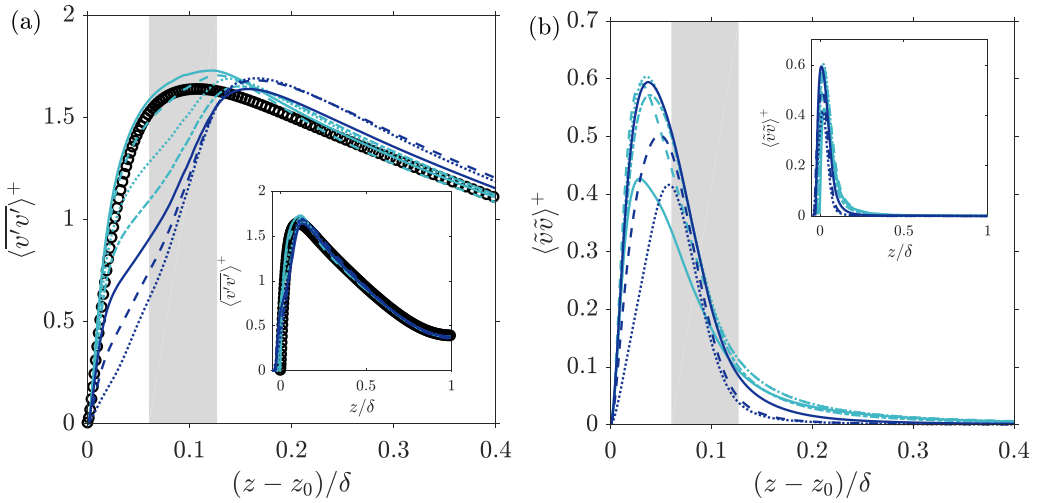

FIG. 9. Spanwise Reynolds (a) and dispersive stresses (b). The area shaded in gray indicates the range of barnacle heights. Line styles for the different coverage cases are given in Table II; black circles indicate smooth-wall data. The areas shaded in gray indicates the range of barnacle heights.

The peak streamwise Reynolds stress occurs around the maximum barnacle height for coverage of 15% or higher. For the 10% coverage case two distinct peaks can be observed: a peak close to maximum barnacle height as for the other cases and an inner, slightly higher, peak located at $(z - z_0)^+ \approx 17$, close to the wall-normal location for the peak location for the streamwise Reynolds stress in the smooth channel reference case. While only a single peak can be observed for the other surfaces, for the low-coverage cases a sharp increase of the streamwise Reynolds stress can be seen close to the location of the inner peak for the 10% case. This feature becomes less pronounced with increasing coverage and fully disappears for the highest-coverage cases (75% and 85%).

The "outer" peak at approximately maximum barnacle height is decreasing for cases with 10%–30% coverage; as coverage is increased further this trend is reversed and an increase in the peak values is observed with the highest peak value occurring for the 85% coverage case; the cases with the lowest peak values thus tend to yield the highest ΔU^+ values. A change in curvature of the profile in the near-wall region from negative, for the more sparsely covered cases, to positive, for the densely covered ones, is visible. This leads to reduced streamwise velocity fluctuations in the near wall region for increased solidity values. A damping of the rms velocity fluctuations with increasing frontal solidity was also observed by MacDonald *et al.* [52]; however, no double peak feature appears in their results. In the study of Leonardi and Castro [26] on regular staggered cube roughness of varying planform (and frontal) solidity a decrease in the streamwise Reynolds stress with increasing solidity within the roughness layer was observed; closely above the roughness the highest solidity surface gave rise to the highest streamwise Reynolds stress values which is consistent with the current observations.

Florens *et al.* [67] performed experiments of flow over roughness with cubical elements with a frontal solidity of 0.19, which corresponds to a 19% coverage at roughness Reynolds number $k_s^+ = 460$. The streamwise normal Reynolds stresses in their experiments increase rapidly in the near-wall region, producing an inner peak, and a higher peak at the cubes' cusp. This behavior is very similar to the barnacle cases with 10% and 15% coverage.

The streamwise dispersive normal stress, $\langle \tilde{u}\tilde{u} \rangle$, corresponds to the spatial variance of the streamwise component of the time-averaged velocity field. As expected, the highest levels of dispersive streamwise normal stress [see Fig. 8(b)] occur below the maximum barnacle height. The maxima of the streamwise dispersive stresses exceed the magnitude of the streamwise Reynolds stress values

for the cases with low coverage, whereas for high coverage, the streamwise dispersive stresses peaks are lower than their Reynolds stress equivalents. The highest peak is observed for the case with 15% coverage and the peak for the 10% coverage case is slightly lower. In the other cases, the maxima of the streamwise dispersive stress profiles show a descending behavior with increasing coverage, with the peak values of the two cases with highest coverage (75% and 85%) having almost identical magnitude. At the same time, the peak location moves further away from the wall indicating that strong interaction between the mean flow and rough surfaces now mainly occurs in the upper part of the rough surface.

The high peak values observed for low-coverage cases are indicative of the dispersive stress definition which quantifies the spatial inhomogeneity in the time-averaged flow produced by the presence of roughness. When more roughness elements are placed on the flat surface, surface roughness becomes more homogeneous and fewer bald patches remain. With low roughness homogeneity and greater sparsity, there is greater local divergence from the mean streamwise velocity values, producing high dispersive stress values. Similar behavior was observed by Leonardi and Castro [26], who found a decrease in the peak value of streamwise dispersive stresses with increasing solidity for regular staggered cube roughness, and Sharma and García-Mayoral [68], who observed a similar decrease in the streamwise dispersive stresses for high frontal solidity for dense filament roughness.

The peak spanwise Reynolds stresses [see Fig. 9(a)] occur around the height of the highest barnacle for the cases with low coverage with a slightly elevated peak level compared to the smooth-wall case. With increasing coverage, the peak location moves above the rough surface and a reduction of spanwise velocity fluctuations can be observed within the rough surface, which is consistent with the decrease in the streamwise velocity fluctuations within the rough surface. In contrast to the results for the streamwise velocity component, the levels of the spanwise dispersive stresses are significantly lower, reaching peak values of less than 40% of the equivalent Reynolds stresses, which is comparable to the levels observed for other forms of irregular roughness [69,70]. As the coverage increases, the peak values first increase before attaining approximately constant levels for the 15% to 60% cases before decreasing again. At the same time, the peak location shifts further away from the surface as coverage is increased.

The spanwise dispersive stresses can be interpreted as a measure for the degree of in-plane circumnavigation of roughness obstacles. For low solidity, large connected smooth patches remain for the current surfaces due to the clustering inherent to the barnacle colonies. Therefore, there is relatively little need for circumnavigation of obstacles and thus spanwise dispersive stress levels are lower. At the same time a barnacle cluster presents a sufficiently large obstacle for the flow to move out of plane and above the barnacles [see also signature for wall-normal dispersive stresses shown in Fig. 10(b)]. On the other end of the solidity range, there is relatively weak streamwise flow within the surface as the obstacles are densely spaced and local channeling of higher velocity fluid occurs. This entails in turn relatively low levels of spanwise dispersive stress. The highest spanwise dispersive stress levels occur thus when there are many roughness obstacles which are still sufficiently widely spaced to be exposed to a strong mean streamwise velocity and which can induce locally significant spanwise motion to the mean flow, i.e., for the current surfaces at the intermediate coverage values.

The behavior of the wall-normal Reynolds stress [see Fig. 10(a)] resembles that of the spanwise Reynolds stress. In the roughness layer, the wall-normal Reynolds stress decreases with increasing coverage; however, compared to the spanwise Reynolds stresses this reduction extends further into the flow. As a result, the peak wall-normal stress occurs for all cases above the highest barnacle height and the peak location moves outwards as coverage increases. The highest peak value can be observed for the 10% coverage case which exceeds the smooth-wall levels. The peak values reduce with increasing coverage attaining an approximately constant value for 60% coverage and above. A monotonous decrease of $\langle\overline{w'w'}\rangle$ with increasing solidity was also observed by Leonardi and Castro [26] for uniform cube roughness and by MacDonald *et al.* [52] for egg-carton roughness, but in their simulations, the peaks occurred closely above the roughness crests and no outwards movement of

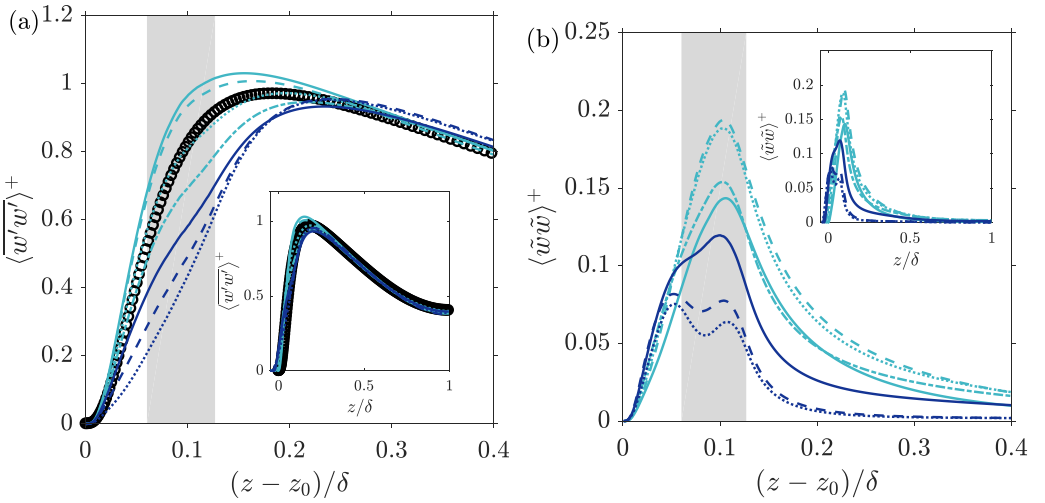

FIG. 10. Wall-normal Reynolds (a) and dispersive stresses (b). Line styles for the different coverage cases are given in Table II; black circles indicate smooth-wall data. The areas shaded in gray indicates the range of barnacle heights.

the peak location with increasing coverage was observed. The differences in peak location trends can be attributed to the nonuniformity of the current surface where there is no single crest location but a distribution of barnacle heights.

The levels attained by the wall-normal dispersive stresses [see Fig. 10(b)] are also significantly lower than for the corresponding Reynolds stresses, an observation that is consistent with results for other irregular rough surfaces [69,70]. It is noticeable that the peak values of the wall-normal stress and the levels sustained above the maximum barnacle height are higher for the lower-coverage surfaces, especially the 15% and 30% coverage cases. This can be attributed to the fact that the low-coverage surfaces have several distinct clusters of barnacles, and each cluster effectively acts as a larger obstacle, encouraging the flow to move on larger, i.e., cluster-scales, over the obstacle. For the high-coverage cases, the clustered nature of the surface increasingly disappears due to merging of clusters, and thus the levels of wall-normal dispersive stress decrease. However, a new feature emerges as coverage increases—a second, inner peak deep within the roughness layer. This peak can be associated with increasing levels of recirculating flow within the gaps the tightly packed barnacles of the high-coverage surfaces and be linked to the net reverse flow observed in the mean streamwise velocity profile deep within the rough surface at high coverage.

The peak for the Reynolds shear stress [see Fig. 11(a)] is located at a higher wall-normal location compared to the smooth-wall reference case in all cases. This is due to significant contributions of the dispersive shear stress in the upper part of the roughness layer. The flow over the 10% coverage case develops the highest Reynolds shear stress peak, located near the maximum barnacle height. As the surface coverage increases the Reynolds shear stress peak decreases and moves further outward. The lowest peak is found at 60% coverage, while the 75% and 85% cases exhibit slightly higher peak values. Within the roughness layer, a strong reduction of the Reynolds shear stress compared to the smooth-wall values can be observed. As the 75% and 85% coverage cases are the ones with reduced roughness function values, compared to the maximum at 60%, it appears that a similar differentiation is only observed over the maximum roughness height and not within the near-wall region, where a monotonous reduction is observed with increasing solidity. The observed near-wall trend with increasing solidity agrees well with the observations by MacDonald *et al.* [52] and Leonardi and Castro [26]. Further away from the wall, the Reynolds shear stress profiles collapse

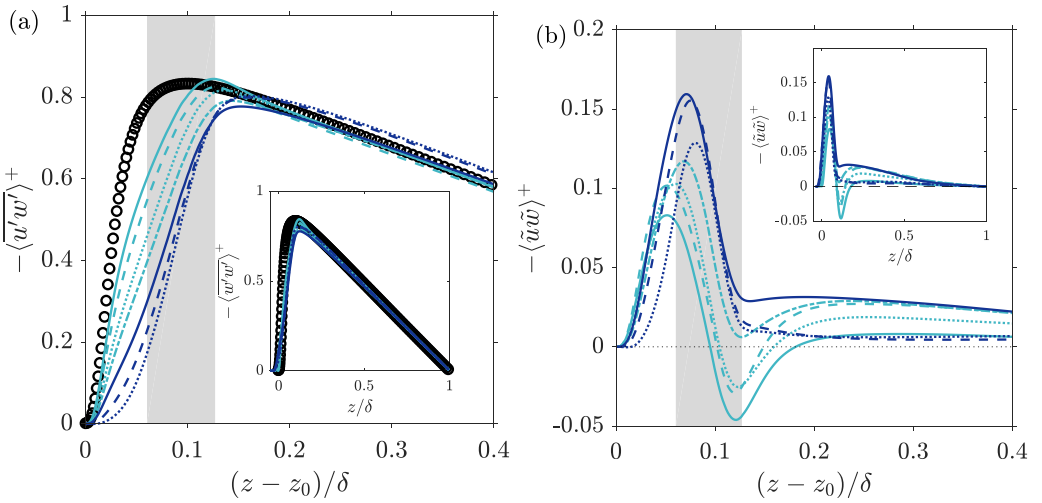

FIG. 11. Reynolds (a) and dispersive (b) shear stresses. Line styles for the different coverage cases are given in Table II; black circles indicate smooth-wall data. The areas shaded in gray indicates the range of barnacle heights.

with the smooth-wall case, showing that the influence of roughness is restricted to the near-wall region [see inset of Fig. 11(a)].

The most complex behavior of all stress profiles considered is exhibited by the dispersive shear stresses [see Fig. 11(b)]. While the absolute levels of the dispersive shear stresses are low, they have a strong impact on the momentum balance in the flow [71]. In all cases, a peak emerges within the roughness layer. The peak moves outwards with increasing coverage; its magnitude increases up to a coverage of 60% and then starts to fall for the 75% and 85% coverage cases; thus the peak value roughly correlates with the roughness function. The profiles for the 75% and 85% cases resemble that of the peaks-only case in Ref. [71] and of the densely covered surfaces studied by Forooghi *et al.* [72]. For low coverage, a characteristic feature emerges in the form of a pronounced minimum located approximately at the maximum barnacle height, leading to negative values of $-\langle\tilde{u}\tilde{w}\rangle$ for the 10%, 15%, and 30% coverage cases. The depth of this minimum decreases with increasing coverage, and no negative values for $-\langle\tilde{u}\tilde{w}\rangle$ are observed for the higher-coverage cases. While, typically, positive values $-\langle\tilde{u}\tilde{w}\rangle$ are reported for rough surfaces, negative values for $-\langle\tilde{u}\tilde{w}\rangle$ have been previously observed in other rough-wall related studies, see, e.g., for flow over superhydrophobic surfaces with streamwise grooves [73] and for irregular rough surfaces with strong spanwise anisotropy [69].

Overall, the dispersive stresses show the presence of inhomogeneities in the time-averaged flow fields, which drop to very low values for $(z-z_0)/\delta \gtrapprox 0.4$. In the recent study by Womack *et al.* [47], secondary flows, which extended to a distance of the order of the boundary layer thickness from the wall, were observed in turbulent boundary layers over surfaces composed of uniformly sized truncated cones in uniform random arrangements. These took the form of high- and low-momentum pathways, similar to those observed in the experimental study by Mejia-Alvarez and Christensen [74] for turbulent boundary layers over a rough surface based on a scan of turbine roughness [75]. For the current case, while there are clear spatial variations in the mean flow fields close to the surfaces, no strong secondary flow structures have been detected that extend to the channel half-height. This may be due to the different roughness configuration. A further possible cause for the absence of strong large-scale secondary flow structures may be the different type of flow configuration: In the present study, turbulent channel flow with roughness on both walls of the channel and periodic boundary conditions in the streamwise and spanwise direction was simulated,

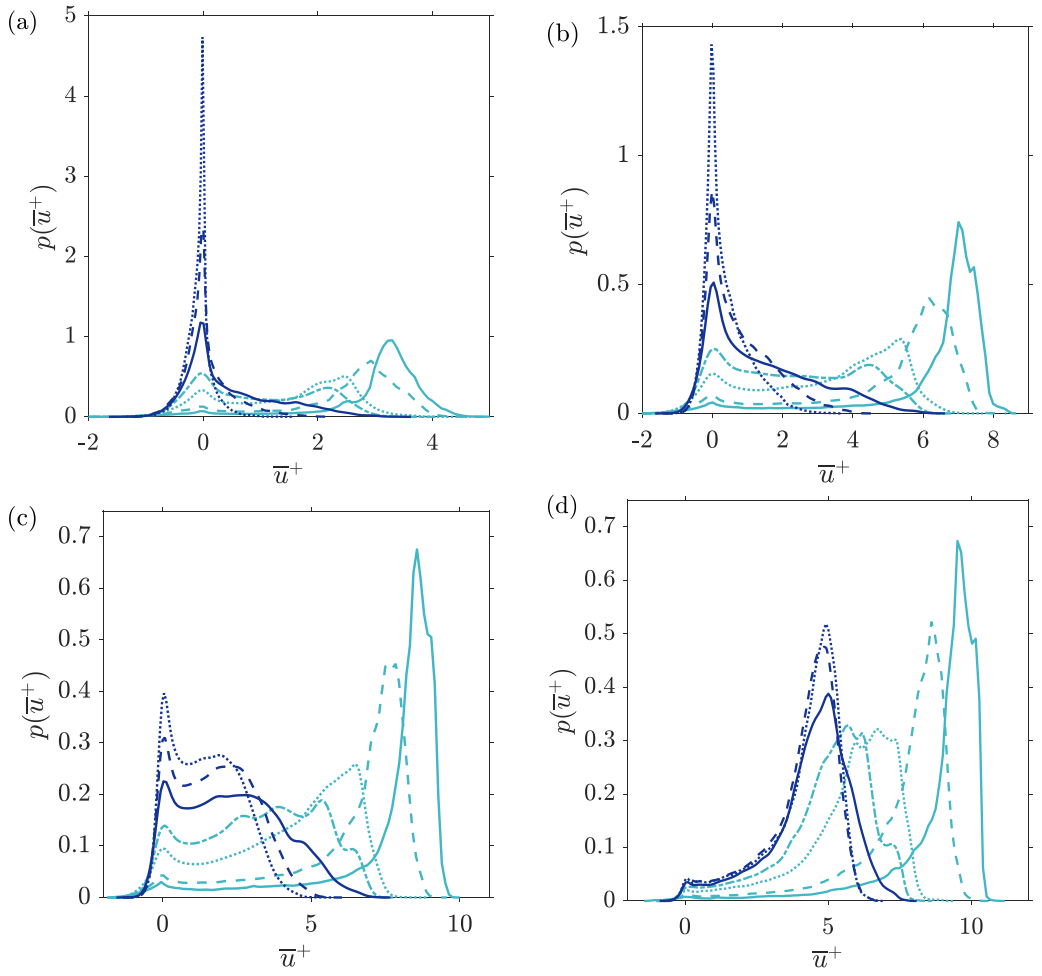

FIG. 12. Comparison of pdfs of the time averaged streamwise velocity component at wall-normal locations (a) $0.1S_{z,\max}$, (b) $0.3S_{z,\max}$, (c) $0.5S_{z,\max}$, and (d) $0.8S_{z,\max}$ above the smooth settling plane. Line styles for the different coverage cases are given in Table II.

whereas the referenced experimental studies used a turbulent boundary layer configuration. This is would be supported by the observation made by Womack *et al.* [47] that in their boundary layer experiments the secondary flows were initiated at the leading edge of the rough surfaces. Per its nature, this initiation mechanism is not possible for turbulent channel flow with periodic boundary conditions, since there is no leading roughness edge. In the following, we therefore focus on the characterisation of the mean flow within the rough surfaces and in their immediate vicinity where clear structures emerge.

D. Analysis of the time-averaged flow field within roughness

The results for the dispersive and Reynolds stress profiles indicate that the flow within the rough surface shows a very strong dependence on the level of coverage. In this section, the time-averaged flow within the rough surface will be analyzed in more detail using probability density functions (pdfs) and flow visualizations of the time-averaged streamwise velocity field $\overline{u}(x, y, z)$ (see Figs. 12–14).

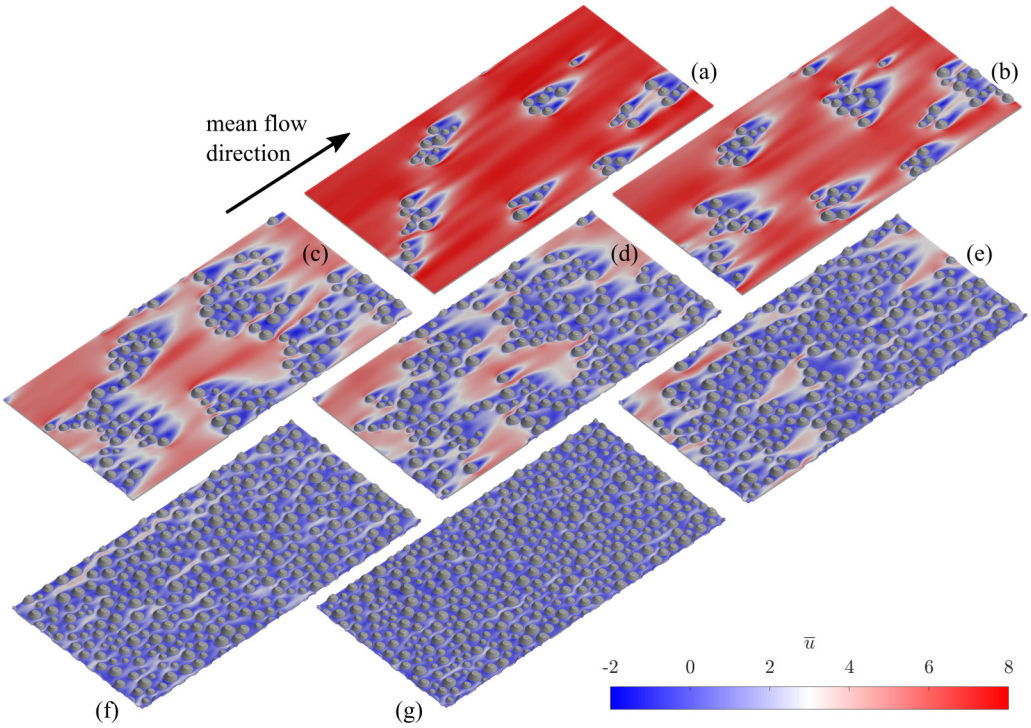

FIG. 13. Time-averaged streamwise velocity field $\overline{u}^+(x, y, z)$ at $0.3S_{z,\max}$ above the smooth settling plane; (a) 10%, (b) 15%, (c) 30%, (d) 45%, (e) 60%, (f) 75%, and (g) 85% coverage.

Pdfs of $\overline{u}$ were sampled at four different wall-normal locations, corresponding $0.1S_{z,\max}$, $0.3S_{z,\max}$, $0.5S_{z,\max}$, and $0.8S_{z,\max}$ above the smooth-wall plane [see Figs. 12(a) to 12(d)]. Deep within the roughness layer [see Figs. 12(a) and 12(b)] there is a high probability for high $\overline{u}$ values at low coverage (10% and 15%), due to the existence of large smooth surface sections over which the flow is free to accelerate in the absence of obstacles [see Figs. 13(a) and 13(b)]. A weak secondary peak is present at $\overline{u} \approx 0$ which can be related to the small velocities in the wake and immediately upstream of the barnacles.

For intermediate coverage (30%, 45%, and 60%), the flow deep within the rough surface becomes increasingly obstructed as the barnacle clusters merge; the pdfs appear quite broad since there is a wide distribution of values for $\overline{u}$. The remaining blank surface patches favor high velocities and, at the same time, the importance of low velocity areas increases due to the higher number of barnacles which entails increased probability of low $\overline{u}$ values in their wakes and in the small gaps between closely spaced barnacles [see Figs. 13(c) to 13(e)].

In contrast, at high coverage (75% and 85%) the pdfs of $\overline{u}$ start to approach the shape of a δ function centered at $\overline{u} = 0$ indicating that the flow deep within the rough surface is largely stagnant. For the 75% coverage case a right-hand tail can be seen, indicating some localized higher mean flow velocities which are a consequence of channeling-like behavior [see Fig. 13(f)]. For the highest coverage of 85%, most of these channels are obstructed by the added barnacles and only weak traces of channeling remain visible [see Fig. 13(g)].

With increasing distance from the smooth-wall plane, i.e., at higher wall-normal locations, the mean of $\overline{u}$ in all cases is shifted to higher values and the pdfs of $\overline{u}$ change their shape depending on the level of surface coverage. For the low-coverage cases (10% and 15%), the pdfs retain approximately the same strongly negatively skewed shape at all wall-normal locations below the maximum roughness height. The appearance of the flow [see Figs. 14(a) and 14(b)] remains

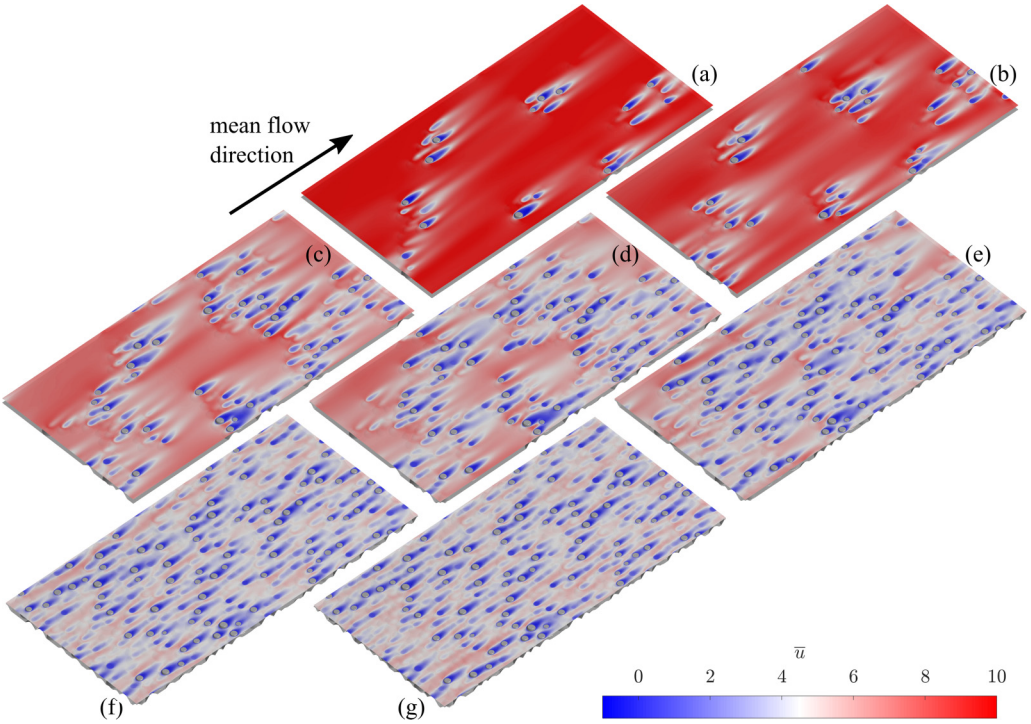

FIG. 14. Time-averaged streamwise velocity field $\overline{u}^+(x, y, z)$ at $0.8S_{z,\max}$ above the smooth settling plane; (a) 10%, (b) 15%, (c) 30%, (d) 45%, (e) 60%, (f) 75%, and (g) 85% coverage.

qualitatively similar to the flow deep within the rough surface [see Fig. 13(a) and 13(b)]; the only significant change is that fewer wake regions remain visible at the higher locations, since the smaller barnacles are submerged.

For intermediate coverage (30%, 45%, and 60%), a broad flat distribution remains visible for $0.3S_{z,\max}$ and $0.5S_{z,\max}$ [see Fig. 12(b) and 12(c)], but toward the upper end of the roughness layer the pdfs start to increasingly resemble the strongly negatively skewed shape of the pdfs for the lower-coverage surfaces [see Fig. 12(d)]. This is because toward the upper end of the roughness layer the appearance of the flow is changed [see Fig. 14(c) to 14(e)], since only the highest barnacles are exposed to the flow, the remaining low velocity areas are closely related to the wakes of the tall exposed barnacles, and large unobstructed areas emerge over which the flow can attain higher $\overline{u}$ values. This explains the change of the pdfs to a more negatively skewed shape.

For the high-coverage cases (75% and 85%) the pdfs undergo the strongest change in shape: For $0.3S_{z,\max}$ [see Fig. 12(b)] the pdfs are strongly positively skewed, and there is still a single dominant peak at $\overline{u} = 0$ which can be associated with nearly stagnant regions of the flow in areas of closely packed barnacles. At 50% of the maximum barnacle height [see Fig. 12(c)] a second peak at $\overline{u} \gg 0$ can be observed, but the pdfs remain positively skewed. Close to the top of the barnacles [see Fig. 12(d)] the peak at $\overline{u} \gg 0$ becomes dominant, the peak at $\overline{u} = 0$ starts to disappear, and the pdfs now have a strongly negatively skewed shape. Since only the highest barnacles remain exposed at $0.8S_{z,\max}$, most are sufficiently distanced from each other to allow the formation of small, individual wakes. The rest of the flow appears relatively uniform; some elongated areas of higher-speed velocity can be discerned which can be directly related to the channels of high speed fluid deeper within the rough surface. These observations explain the strong change in shape in the pdfs for $\overline{u}$ when comparing the pdfs for the $0.3S_{z,\max}$ and $0.8S_{z,\max}$ locations.

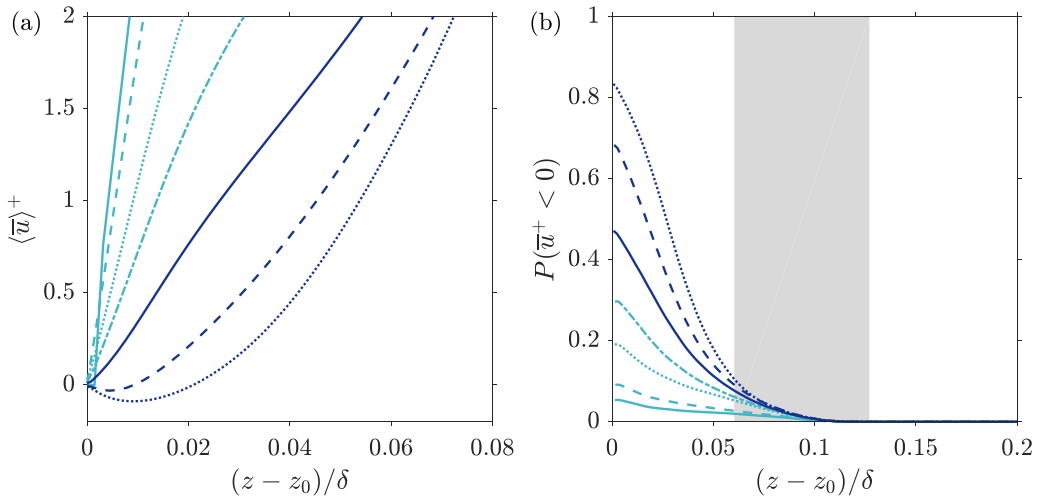

FIG. 15. (a) Mean streamwise velocity profiles within the roughness layer and (b) probability of reverse flow ($\overline{u} < 0$) versus wall-normal location. Line styles for the different coverage cases are given in Table II.

Consequently, the flow behavior can be classified into three categories according to surface coverage: The first category includes surfaces with low barnacle coverage (10% and 15%), where the barnacles form distinct clusters surrounded by large connected areas of smooth surface. In this case, the fluid flows around and above the barnacle clusters, forming connected wake regions. Over the large interconnected smooth surface regions the velocity increases and starts to return to a smooth-wall behavior until the next barnacle cluster is encountered. The second category includes surfaces with medium to high barnacle coverage (30%, 45%, and 60%), where barnacle colonies merge but some smooth surface patches remain. In this case, the fluid experiences much stronger obstruction within the rough surface and can only weakly accelerate over the remaining smooth surface patches that have not yet been colonized by barnacles, with the rest of the flow field within the roughness sublayer being characterized by barnacle wake regions and nearly stagnant velocity regions between closely packed barnacles. The third category contains the heavily covered surfaces (75% and 85% surface coverage), where the barnacles form a single continuous cluster with no large smooth surface patches and only small gaps between barnacles. The flow field in this case appears as a continuous wake field at low wall-normal locations, with the wake of a barnacle being connected to the stagnation areas of the downstream adjacent ones. However, due to the tapered shape of barnacles and their random placement on the smooth surface, irregular streamwise streaks of higher mean velocity can be observed which are the result of a channeling effect. Some traces of this channeling effect remain visible at higher wall-normal locations. The overall behavior of the densely and sparsely covered surfaces resembles the categorization of flow over urban canopy roughness into isolated roughness flow, wake interference flow, and skimming flow, as described by Oke [76].

E. Imprint of the rough surface on the flow

For high-coverage cases, deep within the rough surface, a large fraction of the fluid occupied area is filled with nearly stagnant or recirculating flow. The mean streamwise velocity profile in the immediate vicinity of the wall shows for the 75% and 85% coverage cases a negative mean [see Fig. 15(a)] indicating the predominance of weak reversed flow. This observation is also supported by the probability of reversed flow $\overline{u} < 0$ [see Fig. 15(b)] which reaches values above 0.5 for the 75% and 85% coverage cases as z_0 is approached.

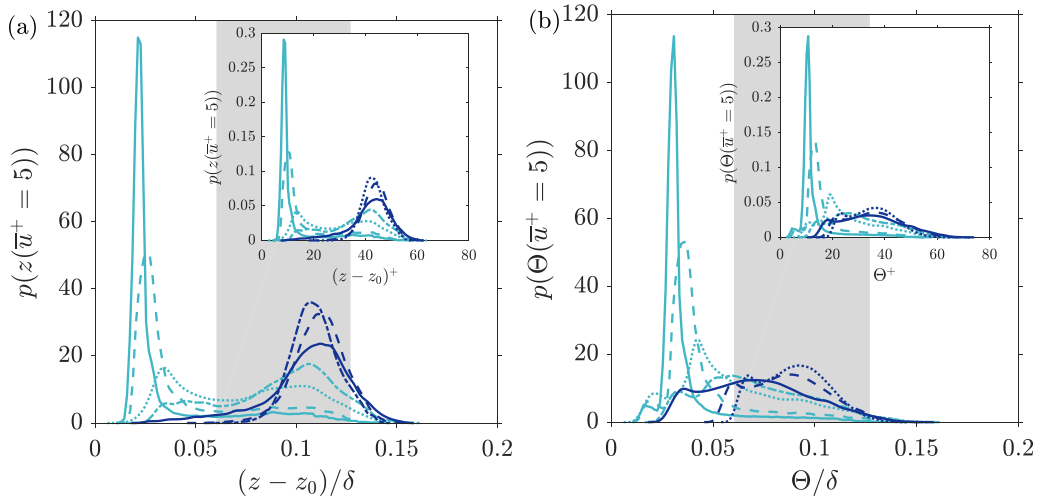

FIG. 16. (a) Pdf of the blanketing layer height and (b) pdf of the blanketing layer thickness Θ. Line styles for the different coverage cases are given in Table II.

Reverse flow areas can have a "cushioning" effect on the flow past a rough surface, since flow tends to skim above areas of recirculating flow [51,71]. For the present surfaces, reverse flow mainly forms in narrow gaps between roughness features and in the near wake of the barnacles. One of the consequences of cushioning is that the flow passing the rough surface effectively interacts only with a reduced frontal area of the roughness elements. The way the "bulk" flow, i.e., the time-averaged flow above the rough surface, experiences the roughness can be quantified using the concept of the "blanketing layer" [51]. The blanketing layer is defined as the isosurface corresponding to $\overline{u}^+(x, y, z) = 5$. This singly connected surface will be referred to by $B(x, y)$ in the following; it should be noted that there is in general no explicit functional expression for $B(x, y)$, i.e., the surface B is in general only implicitly defined.

For a smooth-wall flow, the blanketing layer is a flat plane that is offset by $z^+ = 5$ from the wall and corresponds to the upper end of the viscous sublayer, i.e., $B(x, y) = 5\delta_\nu$ where δ_ν is the viscous length scale of the flow. For rough-wall flows, the concept of the viscous sublayer ceases to exists, and the blanketing layer is strongly shaped by the underlying topography of roughness (see Fig. 17). However, due to processes such as wake formation behind surface peaks and the separation of the mean flow over surface indentations and narrow gaps, the blanketing layer cannot follow the topography of a rough surface perfectly, resulting a distribution of values for the blanketing layer thickness $\Theta = B(x, y) - h(x, y)$ [see Fig. 16(b)]. The blanketing layer thickness for a smooth surface corresponds to a δ function with its peak at $\Theta = 5\delta_\nu$. It can be observed that for the low-coverage cases, some traces of this peak remain visible at low thicknesses which can be associated with the relatively undisturbed flow over the large smooth-wall sections for these surfaces. A right-hand tail to higher thicknesses can be observed as a result of the blanketing layer being further displaced relative to the rough surface in the near wake of the barnacles. For high coverage, there is a broad distribution of values for Θ as a consequence of increasing cushioning of the flow.

While the blanketing layer is a fluid dynamic property characterizing changes in the mean flow induced by the underlying roughness, we can apply approaches from rough surface metrology to characterize its topography. The shape of the blanketing layer has been quantified for each case by computing its topographical parameters in analogy to the topographical parameters for rough surfaces (see Table V). It is immediately apparent by comparing Fig. 17 with Fig. 2 that with increasing coverage the blanketing layer conforms less to the underlying rough surface. This decreasing correlation between height map and blanketing layer can be quantified using the

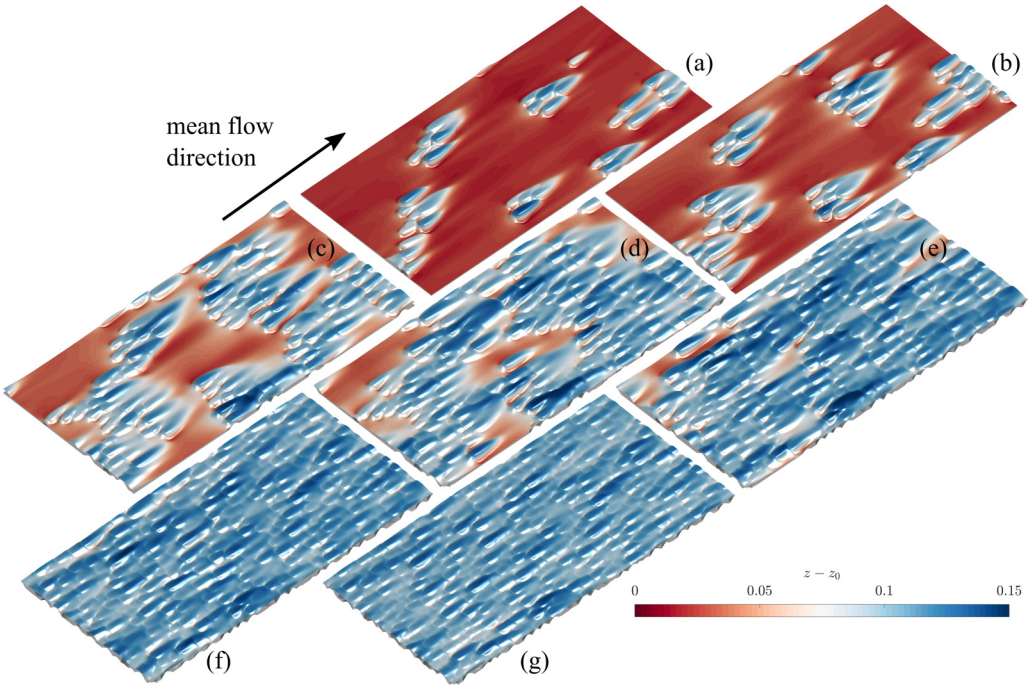

FIG. 17. Three dimensional representation of the blanketing layer for the surfaces with (a) 10%, (b) 15%, (c) 30%, (d) 45%, (e) 60%, (f) 75%, and (g) 85% barnacle coverage.

cross-correlation coefficient between the blanketing layer and the roughness height map which is defined as

$$c_{h,B} = \frac{\langle (B(x,y) - \langle B \rangle)(h(x,y) - \langle h \rangle) \rangle}{(\mathrm{var}(B(x,y))\,\mathrm{var}(h(x,y)))^{1/2}}, \tag{5}$$

where var indicates the variance. Since the flow separates in the wake of the barnacles, there is no perfect correlation between blanketing layer and height map even for the lowest coverage, but the computed value of 0.623 for $c_{h,B}$ indicates a significant correlation between the height map and the blanketing layer at 10% coverage (see Table V). As the coverage increases, from 10% to 75%, $c_{h,B}$

TABLE V. Topographical parameters of the blanketing layer $B(x, y)$, which is implicitly defined by the isosurface $\overline{u}^+(x, y, z) = 5$. λ_f^B, frontal solidity; ES^B, effective slope, S_a^B, mean roughness height; S_q^B, rms roughness height; S_{sk}^B, skewness; S_{ku}^B, kurtosis; $L_{\mathrm{corr}}^{B,x}$, streamwise correlation length; $L_{\mathrm{corr}}^{B,y}$, spanwise correlation length; $\langle B \rangle - z_0$, mean height above smooth wall; $\min(B) - z_0$, minimum height of the blanketing layer above the smooth surface; $c_{h,B}$, cross-correlation coefficient between $h(x, y)$ and $B(x, y)$.

Coverage	λ_f^B	ES^B	S_a^B/δ	S_q^B/δ	S_{sk}^B	S_{ku}^B	$L_{\mathrm{corr}}^{B,x}/\delta$	$L_{\mathrm{corr}}^{B,y}/\delta$	$(\langle B \rangle - z_0)/\delta$	$(\min(B) - z_0)/\delta$	$c_{h,B}$
10%	0.022	0.044	0.019	0.027	1.99	5.74	0.68	0.32	0.035	0.012	0.623
15%	0.031	0.061	0.025	0.030	1.22	3.12	0.66	0.39	0.046	0.013	0.576
30%	0.041	0.081	0.028	0.032	0.08	1.76	0.81	0.48	0.074	0.017	0.492
45%	0.043	0.085	0.023	0.028	-0.48	2.38	0.97	0.39	0.091	0.023	0.420
60%	0.042	0.085	0.016	0.021	-1.00	4.31	1.03	0.15	0.105	0.022	0.317
75%	0.038	0.077	0.010	0.013	-0.33	3.50	0.53	0.09	0.111	0.049	0.236
85%	0.035	0.069	0.009	0.011	0.075	3.02	0.47	0.08	0.109	0.057	0.255

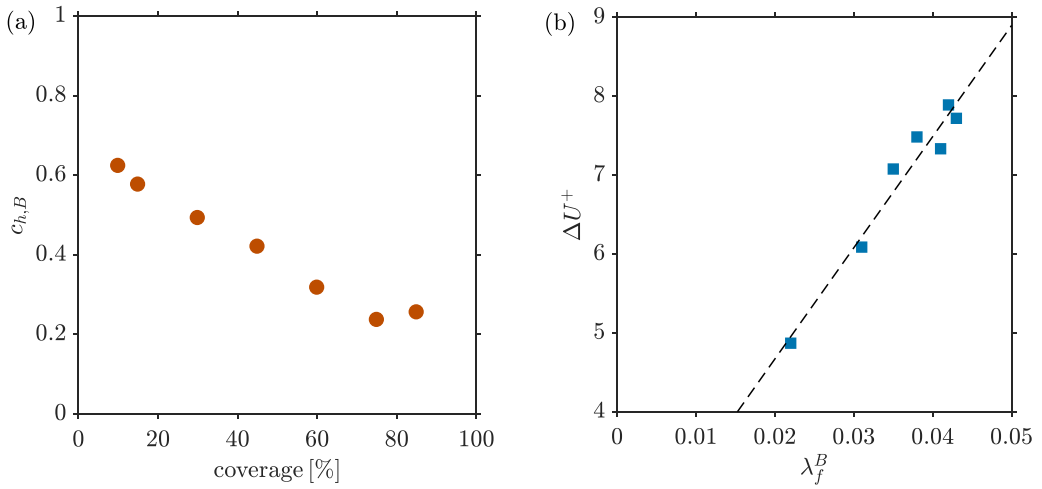

FIG. 18. (a) Cross-correlation coefficient $c_{h,B}$ as a function of coverage; (b) ΔU^+ as a function of the frontal solidity of the blanketing layer. The fitted line corresponds to $f(\lambda_f^B) = 140.9\,\lambda_f^B + 1.851$.

decreases. A slight increase can be observed for the highest coverage (85%) compared to the 75% case [see Fig. 18(a)]. Due to the irregular nature of the rough surfaces, the slightly higher value of the 85% case cannot be related to any specific feature of this surface. For very high coverage, the cross-correlation may show an increasing trend due to the increased solidity of the surfaces. For example, for a roughness composed of uniform cubes, a cross-correlation coefficient of 1 should be approached in the limit of 100% coverage, where all the cubes merge to form a new flat solid surface. Since the current roughness elements are nonuniform in height and tapering, this limit will not be attained but the effect may be sufficient to cause the observed increase in the cross-correlation coefficient.

For low to medium coverage, the blanketing layer mean height moves further away from the smooth reference surface but it attains an approximately constant value for 60% coverage and above. The spatial structure of the blanketing layer also changes with increasing coverage: For moderate coverage (15% and 30%), it is nearly isotropic, i.e., the streamwise and spanwise correlation length are of similar magnitude. As coverage is increased further, the blanketing layer starts to be dominated by elongated structures which can be related to the wake-interference phenomenon discussed above, where the distinct character of the wakes of individual barnacle roughness elements gets lost due to merging of wakes. The kurtosis value of the blanketing layer S_{ku}^B drops with increasing skewness from a moderately high value to a Gaussian value of approximately 3; comparing these values to the corresponding topographical parameters for the underlying rough surfaces it is apparent that both the extremely high and low kurtosis values are attenuated by the cushioning effect. The skewness values are also influenced by the cushioning; in all cases, the $S_{\mathrm{sk}}^B < S_{\mathrm{sk}}$, i.e., due to the wake formation the barnacle roughness elements appear as less pronounced peaks to the outer flow. For medium to high coverage, the blanketing layer surface ceases to be peak dominated and it exhibits negative skewness values due to the emerging streamwise narrow valleys that can be associated with the channelling effect. As the channeling effect starts to weaken at the highest coverage, the skewness of the blanketing layer approaches zero, i.e., the blanketing layer starts to resemble a Gaussian surface.

Finally, the frontal solidity and effective slope of the blanketing layer give rise to an interesting observation: With increasing coverage the frontal solidity/effective slope of $B(x, y)$ first rises, reaching its maximum at 45% and 60%, and then decreases at 75% and 85% coverage. The blanketing layer thus gives direct insight into the question why ΔU^+ decreases for high frontal

solidity; this happens because the solidity of the surface perceived by the bulk flow (here quantified using the blanketing layer) starts to decrease [see Fig. 18(b)].

IV. CONCLUSIONS

The fluid dynamic behavior of barnacle-type rough surfaces with increasing coverage was investigated using direct numerical simulations of turbulent channel flow at $\mathrm{Re}_\tau = 395$. While the present surfaces were inspired by a typical form of marine biofouling, barnacle-type roughness can also serve as a general example for irregular roughness composed of roughness elements of randomized height and shape. Unlike the more homogeneous regular and irregular rough surfaces considered in most previous investigations of the fundamental properties of rough-wall turbulence, the current barnacle-type rough surfaces are characterized by clustering of roughness features at low plan-form solidity. This leads to some distinct behavior at low coverage, as traces of smooth wall behavior are recovered over the large connected smooth section that are characteristic of these surfaces. Analogies between the present surfaces and other forms of roughness can be made to urban flows, as the observed mean flow behavior essentially follows the categorisation of Oke [76].

The roughness function followed the expected trend with frontal solidity but did not exhibit the expected saturation of the roughness effect with high effective slope. The decrease at high effective slope reinforces that other topographical parameters, such as skewness, also have a strong influence on the roughness effect (see discussion in Ref. [46]). However, when considering the "perceived" roughness from the perspective of the flow that passes over roughness, here quantified using the blanketing layer, a simpler behavior emerges, namely a linear increase in the roughness function with increasing effective slope of the blanketing layer. It remains to be established whether this would also apply for other forms of roughness. If a reliable mapping between rough surface and blanketing layer topography could be achieved, then simpler relationships between topographical parameters and the roughness effect may emerge. However, due to the complex nature of separation and reattachment over a rough surface, the emergence of channeling within the roughness, as well as the wide range of roughness topographies encountered in engineering and geophysical applications, a general mapping may be difficult to achieve.

Roughness height maps and velocity statistics are available in .csv format [77].

ACKNOWLEDGMENTS

We gratefully acknowledge support by the United Kingdom Engineering and Physical Sciences Research Council (EPSRC) [Grant No. EP/P009875/1]. This work used the ARCHER UK National Supercomputing Service (http://www.archer.ac.uk).

[1] J. A. Lewis, Marine biofouling and its prevention on underwater surfaces, Mater. Forum **22**, 41 (1998).
[2] Woods Hole Oceanographic Institution, *Marine Biofouling and Its Prevention* (U.S. Naval Institute, Annapolis, MD, 1952).
[3] S. M. Evans, A. C. Birchenough, and M. S. Brancato, The TBT ban: Out of the frying pan into the fire? Mar. Pollut. Bull. **40**, 204 (2000).
[4] L. Gipperth, The legal design of the international and European Union ban on tributyltin antifouling paint: Direct and indirect effects, J. Environ. Manage. **90**, S86 (2009).
[5] M. Salta, L. Chambers, J. Wharton, R. Wood, J. F. Briand, Y. Blache, and K. R. Stokes, Marine fouling organisms and their use in antifouling bioassays, in *Proceedings of the European Corrosion Congress (EUROCORR'09), Nice, France* (CEFRACOR, Paris, 2009).
[6] M. P. Schultz and G. W. Swain, The influence of biofilms on skin friction drag, Biofouling **15**, 129 (2000).

[7] M. P. Schultz, Turbulent boundary layers on surfaces covered with filamentous algae, J. Fluids Eng. **122**, 357 (2000).
[8] M. P. Schultz, Frictional resistance of antifouling coating systems, J. Fluids Eng. **126**, 1039 (2004).
[9] J. Barros, E. Murphy, and M. P. Schultz, Particle image velocimetry measurements of the flow over barnacles in a turbulent boundary layer, in *Proceedings of the 18th International Symposium of the Application of Laser and Imaging Techniques to Fluid Mechanics, Lisbon, Portugal* (TEchnio, Lisboa, 2016).
[10] J. P. Monty, E. Dogan, R. Hanson, A. J. Scardino, B. Ganapathisubramani, and N. Hutchins, An assessment of the ship drag penalty arising from light calcareous tubeworm fouling, Biofouling **32**, 451 (2016).
[11] K. M. Berntsson and P. R. Jonsson, Temporal and spatial patterns in recruitment and succession of a temperate marine fouling assemblage: A comparison of static panels and boat hulls during the boating season, Biofouling **19**, 187 (2003).
[12] R. L. Townsin, The ship fouling penalty, Biofouling **19**, 9 (2003).
[13] J. Loxton, A. K. Macleod, C. R. Nall, T. McCollin, I. Machado, T. Simas, T. Vance, C. Kenny, A. Want, and R. G. Miller, Setting an agenda for biofouling research for the marine renewable energy industry, Int. J. Mar. Energy **19**, 292 (2017).
[14] C. C. Stringer and B. L. Polyage, Implications of biofouling on cross-flow turbine performance, SN Appl. Sci. **2**, 464 (2020).
[15] J.S. Walker, R. B. Green, E. A. Gillies, and C. Phillips, The effect of a barnacle-shaped excrescence on the hydrodynamic performance of a tidal turbine blade section, Ocean Eng. **217**, 107849 (2020).
[16] M. P. Schultz, J. A. Bendick, E. R. Holm, and W. M. Hertel, Economic impact of biofouling on a naval surface ship, Biofouling **27**, 87 (2011).
[17] Y. K. Demirel, O. Turan, and A. Incesik, Predicting the effect of biofouling on ship resistance using CFD, Appl. Ocean Res. **62**, 100 (2017).
[18] Y. K. Demirel, D. Uzun, Y. Zhang, H.-C. Fang, A. H. Day, and O. Turan, Effect of barnacle fouling on ship resistance and powering, Biofouling **33**, 819 (2017).
[19] D. Uzun, Y. Zhang, Y. K. Demirel, and O. Turan, Experimental determination of added resistance due to barnacle fouling of ships by using 3d printed barnacles, in *Proceedings of the 5th International Conference on Advanced Measurement Technology for the Maritime Industry (AMT'17), Glasgow, UK* (University of Strathclyde, Glasgow, 2017).
[20] F. R. Hama, Boundary-layer Characteristics for Smooth and Rough Surfaces, Transactions of the Society for Naval Architects and Marine Engineers **62**, 333 (1954).
[21] J. A. C. Orme, I. Masters, and R. T. Griffiths, Investigation of the effect of biofouling on the efficiency of marine current turbines, in *MAREC 2001*, edited by C. French (Institute of Marine Engineers, Mumbai, India, 2001), pp. 91–99.
[22] Jasim Sadique, Turbulent flows over macro-scale roughness elements—from biofouling barnacles to urban canopies, Ph.D. thesis, John Hopkins University, Baltimore, Maryland, 2016.
[23] D. Kong, C. Dong, Z. Zheng, F. Mao, A. Xu, X. Ni, C. Man, J. Yao, K. Xiao, and X. Li, Surface monitoring for pitting evolution into uniform corrosion on cu-ni-zn ternary alloy in alkaline chloride solution: Ex-situ LCM and in-situ SECM, Appl. Surf. Sci. **440**, 245 (2018).
[24] H. Schlichting, Experimental investigation of the problem of surface roughness, Ingen.-Arch. **7**, 1 (1937).
[25] O. Coceal, T. G. Thomas, and S. E. Belcher, Spatial variability of flow statistics within regular building arrays, Bound.-Layer Meteorol. **125**, 537 (2007).
[26] S. Leonardi and I. P. Castro, Channel flow over large cube roughness: A direct numerical simulation study, J. Fluid Mech. **651**, 519 (2010).
[27] K. A. Flack and M. P. Schultz, Roughness effects on wall-bounded turbulent flows, Phys. Fluids **26**, 101305 (2014).
[28] Y. K. Choi, H. G. Hwang, Y. M. Lee, and J. H. Lee, Effects of the roughness height in turbulent boundary layers over rod- and cuboid-roughened walls, Int. J. Heat Fluid Flow **85**, 108644 (2020).
[29] J. Nikuradse, Laws of flow in rough pipes, VDI Forschungsheft **361**, 1 (1933).

[30] R. Mejia-Alvarez and K. T. Christensen, Low-order representations of irregular surface roughness and their impact on a turbulent boundary layer, Phys. Fluids **22**, 015106 (2010).
[31] J. Yuan and P. Piomelli, Estimation and prediction of the roughness function on realistic surfaces, J. Turbul. **15**, 350 (2014).
[32] M. Thakkar, A. Busse, and N. D. Sandham, Surface correlations of hydrodynamic drag for transitionally rough engineering surfaces, J. Turbul. **18**, 138 (2016).
[33] P. Forooghi, A. Stroh, F. Magagnato, S. Jakirlić, and B. Frohnapfel, Toward a universal roughness correlation, J. Fluids Eng. **139**, 121201 (2017).
[34] Y. Kuwata and Y. Kawaguchi, Direct numerical simulation of turbulence over systematically varied irregular rough surfaces, J. Fluid Mech. **862**, 781 (2019).
[35] B. Nugroho, J. P. Monty, I. K. A. P. Utama, B. Ganapathisubramani, and N. Hutchins, Non–type behaviour of roughness when in-plane wavelength approaches the boundary layer thickness, J. Fluid Mech. **911**, A1 (2021).
[36] F. Alves Portela, A. Busse, and N. D. Sandham, Numerical study of fourier-filtered rough surfaces, Phys. Rev. Fluids **6**, 084606 (2021).
[37] Charles Darwin, *A Monograph on the Sub-class Cirripedia, with Figures of All the Species* (The Ray Society, London, 1854).
[38] E. W. Knight-Jones, Laboratory experiments on gregariousness during setting in Balanus balanoides and other barnacles, J. Exp. Biol. **30**, 584 (1953).
[39] E. W. Knight-Jones and D. J. Crisp, Gregariousness in barnacles in relation to the fouling of ships and to anti-fouling research, Nature (Lond.) **171**, 1109 (1953).
[40] D. J. Crisp, The behaviour of barnacle cyprids in relation to water movement over a surface, J. Exp. Biol. **32**, 569 (1955).
[41] L. S. Mullineaux and C. A. Butman, Initial contact, exploration and attachment of barnacle (balanus amphitrite) cyprids settling in flow, Mar. Biol. **110**, 93 (1991).
[42] K. C. Chaw and W. R. Birch, Quantifying the exploratory behaviour of Amphibalanus amphitrite cyprids, Biofouling **25**, 611 (2009).
[43] Sotirios Sarakinos and Angela Busse, An algorithm for the generation of biofouled surfaces for application in marine hydrodynamics, in *Progress in CFD for Wind and Tidal Offshore Turbines*, edited by Esteban Ferrer and Adeline de Montlaur (Springer, Berlin, 2019).
[44] K. Pearson, IX. Mathematical contributions to the theory of evolution. XIX. Second supplement to a memoir on skew variation, Phys. Trans. Roy. Soc. London A **216**, 429 (1916).
[45] E. Napoli, V. Armenio, and M. De Marchis, The effect of slope of irregularly distributed roughness elements on turbulent wall-bounded flows, J. Fluid Mech. **613**, 385 (2008).
[46] D. Chung, N. Hutchins, M. P. Schultz, and K. A. Flack, Predicting the drag of rough surfaces, Annu. Rev. Fluid Mech. **53**, 439 (2021).
[47] K. M. Womack, R. J. Volino, C. Meneveau, and M. P. Schultz, Turbulent boundary layer flow over regularly and irregularly arranged truncated cone surfaces, J. Fluid Mech. **933**, A38 (2022).
[48] A. Busse, M. Lützner, and N. D. Sandham, Direct numerical simulations of turbulent flow over rough surface based on a surface scan, Comput. Fluids **116**, 129 (2015).
[49] J. Yang and E. Balaras, An embedded-boundary formulation for large-eddy simulation of turbulent flows interacting with moving boundaries, J. Comput. Phys. **215**, 12 (2006).
[50] L. Chan, M. MacDonald, D. Chung, N. Hutchins, and A. Ooi, A systematic investigation of roughness height and wavelength in turbulent pipe flow in the transitionally rough regime, J. Fluid Mech. **771**, 743 (2015).
[51] A. Busse, M. Thakkar, and N. D. Sandham, Reynolds-number dependence of the near-wall flow over irregular rough surfaces, J. Fluid Mech. **810**, 196 (2017).
[52] M. MacDonald, L. Chan, D. Chung, N. Hutchins, and A. Ooi, Turbulent flow over transitionally rough surfaces with varying roughness densities, J. Fluid Mech. **804**, 130 (2016).
[53] M. P. Schultz and K. A. Flack, Turbulent boundary layers on a systematically varied rough wall, Phys. Fluids **21**, 015104 (2009).
[54] J. Jiménez, Turbulent flows over rough walls, Annu. Rev. Fluid Mech. **36**, 173 (2004).

[55] R. L. Webb, E. R. G. Eckert, and R. J. Goldstein, Heat transfer and friction in tubes with repeated-rib roughness, Int. J. Heat Mass Transf. **14**, 601 (1971).
[56] I. Tani, Turbulent boundary layer development over rough surfaces, in *Perspectives in Turbulence Studies*, edited by H. U. Meier and P. Bradshaw (Spinger-Verlag, Berlin, 1987), pp. 223–249.
[57] P. R. Bandyopadhyay, Rough-wall turbulent boundary layers in the transition regime, J. Fluid Mech. **180**, 231 (1987).
[58] M. Placidi and B. Ganapathisubramani, Effects of frontal and plan solidities on aerodynamic parameters and the roughness sublayer in turbulent boundary layers, J. Fluid Mech. **782**, 541 (2015).
[59] K. A. Flack, M. P. Schultz, and J. M. Barros, Skin friction measurements of systematically-varied roughness: Probing the role of roughness amplitude and skewness, Flow, Turbul. Combust. **104**, 317 (2019).
[60] W. K. George, Is there a universal log law for turbulent wall-bounded flows? Philos. Trans. Roy. Soc. A **365**, 789 (2007).
[61] J. J. Finnigan, Turbulence in plant canopies, Annu. Rev. Fluid Mech. **32**, 519 (2000).
[62] A. Sharma and R. García-Mayoral, Scaling and dynamics of turbulence over sparse canopies, J. Fluid Mech. **888**, A1 (2020).
[63] A. Busse and N. D. Sandham, Parametric forcing approach to rough-wall turbulent channel flow, J. Fluid Mech. **712**, 169 (2012).
[64] P. Forooghi, B. Frohnapfel, F. Magagnato, and A. Busse, A modified parametric forcing approach for modelling of roughness, Int. J. Heat Fluid Flow **71**, 200 (2018).
[65] H. Cheng and I. P. Castro, Near wall flow over urban-line roughness, Bound.-Layer Meteorol. **104**, 229 (2002).
[66] M. R. Raupach and R. H. Shaw, Averaging procedures for flow within vegetation canopies, Bound.-Layer Meteorol. **22**, 79 (1982).
[67] E. Florens, O. Eiff, and F. Moulin, Defining the roughness sublayer and its turbulence statistics, Exp. Fluids **54**, 1500 (2013).
[68] A. Sharma and R. García-Mayoral, Turbulent flows over dense filament canopies, J. Fluid Mech. **888**, A2 (2020).
[69] A. Busse and T. O. Jelly, Influence of surface anisotropy on turbulent flow over irregular roughness, Flow Turbul. Combust. **104**, 331 (2019).
[70] T. O. Jelly and A. Busse, Reynolds number dependence of Reynolds and dispersive stresses in turbulent channel flow past irregular near-Gaussian roughness, Int. J. Heat Fluid Flow **80**, 108485 (2019).
[71] T. O. Jelly and A. Busse, Reynolds and dispersive shear stress contributions above highly skewed roughness, J. Fluid Mech. **852**, 710 (2018).
[72] P. Forooghi, A. Stroh, P. Schlatter, and B. Frohnapfel, Direct numerical simulation of flow over dissimilar, randomly distributed roughness elements: A systematic study on the effect of surface morphology on turbulence, Phys. Rev. Fluids **3**, 044605 (2018).
[73] S. Türk, G. Daschiel, A. Stroh, Y. Hasegawa, and B. Frohnapfel, Turbulent flow over superhydrophobic surfaces with streamwise grooves, J. Fluid Mech. **747**, 186 (2014).
[74] R. Mejia-Alvarez and K. T. Christensen, Wall-parallel stereo particle-image velocimetry measurements in the roughness sublayer of turbulent flow overlying highly irregular roughness, Phys. Fluids **25**, 115109 (2013).
[75] J. P. Bons, R. P. Taylor, S. T. McClain, and R. B. Rivir, The many faces of turbine surface roughness, J. Turbomachin. **123**, 739 (2001).
[76] T. R. Oke, Street design and urban canopy layer climate, Energy Build. **11**, 103 (1988).
[77] http://dx.doi.org/10.5525/gla.researchdata.1288.